Article

Developmental Cell

MYO10-filopodia support basement membranes at pre-invasive tumor boundaries

Graphical abstract

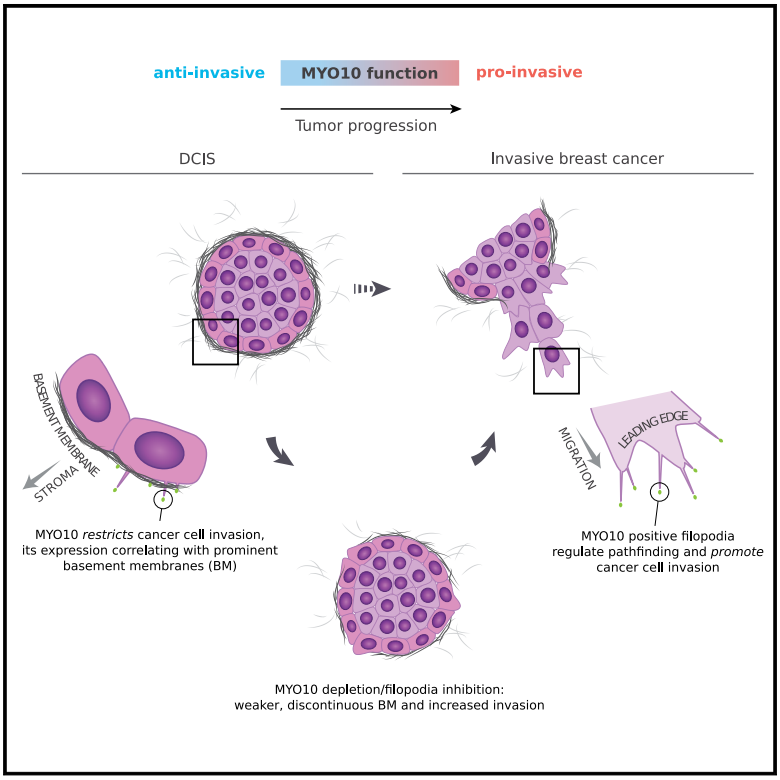

Highlights

- MYO10 expression is elevated at the ductal carcinoma *in situ* (DCIS) breast cancer stage
- MYO10 expression correlates with basement membrane (BM) assembly in DCIS-like xenografts
- Loss of MYO10-dependent filopodia impairs BM and induces an EMT-like phenotype *in vivo*
- MYO10 filopodia positively correlate with fibronectin assembly *in vitro* and *in vivo*

Authors

Emilia Peuhu, Guillaume Jacquemet, Colinda L.G.J. Scheele, ..., Pauliina Hartiala, Jacco van Rheenen, Johanna Ivaska

Correspondence

emilia.peuhu@utu.fi (E.P.), guillaume.jacquemet@abo.fi (G.J.), johanna.ivaska@utu.fi (J.I.)

In brief

Peuhu, Jacquemet, et al. investigate the role of myosin-X filopodia during breast cancer progression. They report that myosin-X filopodia are protective at the early stage of the disease, contributing to basement membrane integrity, but are pro-invasive at later stages, facilitating cancer-cell dissemination.

Peuhu et al., 2022, Developmental Cell *57*, 2350–2364
October 24, 2022
https://doi.org/10.1016/j.devcel.2022.09.016

CellPress

CellPress
OPEN ACCESS

Developmental Cell

Article

MYO10-filopodia support basement membranes at pre-invasive tumor boundaries

Emilia Peuhu,[1,2,15,*] Guillaume Jacquemet,[2,3,4,5,15,*] Colinda L.G.J. Scheele,[6,7] Aleksi Isomursu,[2] Marie-Catherine Laisne,[2,3] Leena M. Koskinen,[1,2] Ilkka Paatero,[2] Kerstin Thol,[2] Maria Georgiadou,[2] Camilo Guzmán,[2] Satu Koskinen,[2] Asta Laiho,[2] Laura L. Elo,[1,2,8] Pia Boström,[9,10] Pauliina Hartiala,[10,11] Jacco van Rheenen,[6] and Johanna Ivaska[2,8,12,13,14,16,*]

[1]Institute of Biomedicine and FICAN West Cancer Centre Laboratory, University of Turku, 20520 Turku, Finland
[2]Turku Bioscience Centre, University of Turku and Åbo Akademi University, 20520 Turku, Finland
[3]Åbo Akademi University, Faculty of Science and Engineering, Biosciences, 20520 Turku, Finland
[4]Turku Bioimaging, University of Turku and Åbo Akademi University, 20520 Turku, Finland
[5]InFLAMES Research Flagship Center, Åbo Akademi University, 20520 Turku, Finland
[6]Division of Molecular Pathology, Oncode Institute-Netherlands Cancer Institute, 1066CX Amsterdam, the Netherlands
[7]VIB-KU Leuven Center for Cancer Biology, Department of Oncology, 3000 Leuven, Belgium
[8]InFLAMES Research Flagship Center, University of Turku, 20520 Turku, Finland
[9]Department of Pathology, Turku University Hospital, 20520 Turku, Finland
[10]University of Turku, 20520 Turku, Finland
[11]Department of Plastic and General Surgery, Turku University Hospital, 20520 Turku, Finland
[12]Department of Life Technologies, University of Turku, 20520 Turku, Finland
[13]Western Finnish Cancer Center (FICAN West), University of Turku, FI-20520 Turku, Finland
[14]Foundation for the Finnish Cancer Institute, Tukholmankatu 8, FI-00014 Helsinki, Finland
[15]These authors contributed equally
[16]Lead contact
*Correspondence: emilia.peuhu@utu.fi (E.P.), guillaume.jacquemet@abo.fi (G.J.), johanna.ivaska@utu.fi (J.I.)
https://doi.org/10.1016/j.devcel.2022.09.016

SUMMARY

Ductal carcinoma *in situ* (DCIS) is a pre-invasive stage of breast cancer. During invasion, the encapsulating DCIS basement membrane (BM) is compromised, and tumor cells invade the surrounding stroma. The mechanisms that regulate functional epithelial BMs *in vivo* are poorly understood. Myosin-X (MYO10) is a filopodia-inducing protein associated with metastasis and poor clinical outcome in invasive breast cancer (IBC). We identify elevated MYO10 expression in human DCIS and IBC, and this suggests links with disease progression. MYO10 promotes filopodia formation and cell invasion *in vitro* and cancer-cell dissemination from progressively invasive human DCIS xenografts. However, MYO10-depleted xenografts are more invasive. These lesions exhibit compromised BMs, poorly defined borders, and increased cancer-cell dispersal and EMT-marker-positive cells. In addition, cancer spheroids are dependent on MYO10-filopodia to generate a near-continuous extracellular matrix boundary. Thus, MYO10 is protective in early-stage breast cancer, correlating with tumor-limiting BMs, and pro-invasive at later stages, facilitating cancer-cell dissemination.

INTRODUCTION

Despite recent therapeutic advances, breast cancer remains a significant cause of death among women (Ferlay et al., 2018). Breast cancer is particularly impervious to established therapies at the later stages of the disease when tumors have become invasive and metastatic. A critical step in breast cancer progression is transitioning from ductal carcinoma *in situ* (DCIS) to invasive breast cancer (IBC). DCIS is surrounded by a basement membrane (BM), acting as a barrier between the epithelial cells and the surrounding stroma. The transition to IBC typically involves cancer cells breaching this BM barrier to invade the surrounding tissue, either as single cells or as a stream (Clark and Vignjevic, 2015), such that, in IBC, the BM is generally absent. DCIS is considered a benign tumor but also a non-obligate precursor of IBC, and thus, a significant proportion of patients with DCIS eventually progress to IBC (Betsill et al., 1978; Ryser et al., 2019). Therefore, understanding how cancer cells interact with and breach the BM is of high clinical and therapeutic interest.

BMs are thin, dense sheets of specialized extracellular matrix (ECM) molecules surrounding epithelial tissues (Yurchenco and Patton, 2009). They are composed of a three-layer ECM network, the inner layer mainly containing laminins, and the outer layer formed of type IV collagen. These two layers are interlinked by several additional ECM molecules, including nidogen, lumican, and perlecan. BMs are effective biological barriers maintained by constant turnover and remodeling of ECM components (Keeley et al., 2020; Matsubayashi et al., 2020). In addition, BMs regulate epithelial architecture by establishing polarity and by providing survival and differentiation cues and mechanical support.

Cancer cells can utilize specialized protrusions, such as invadopodia to traverse BMs (Eddy et al., 2017). Invadopodia contain

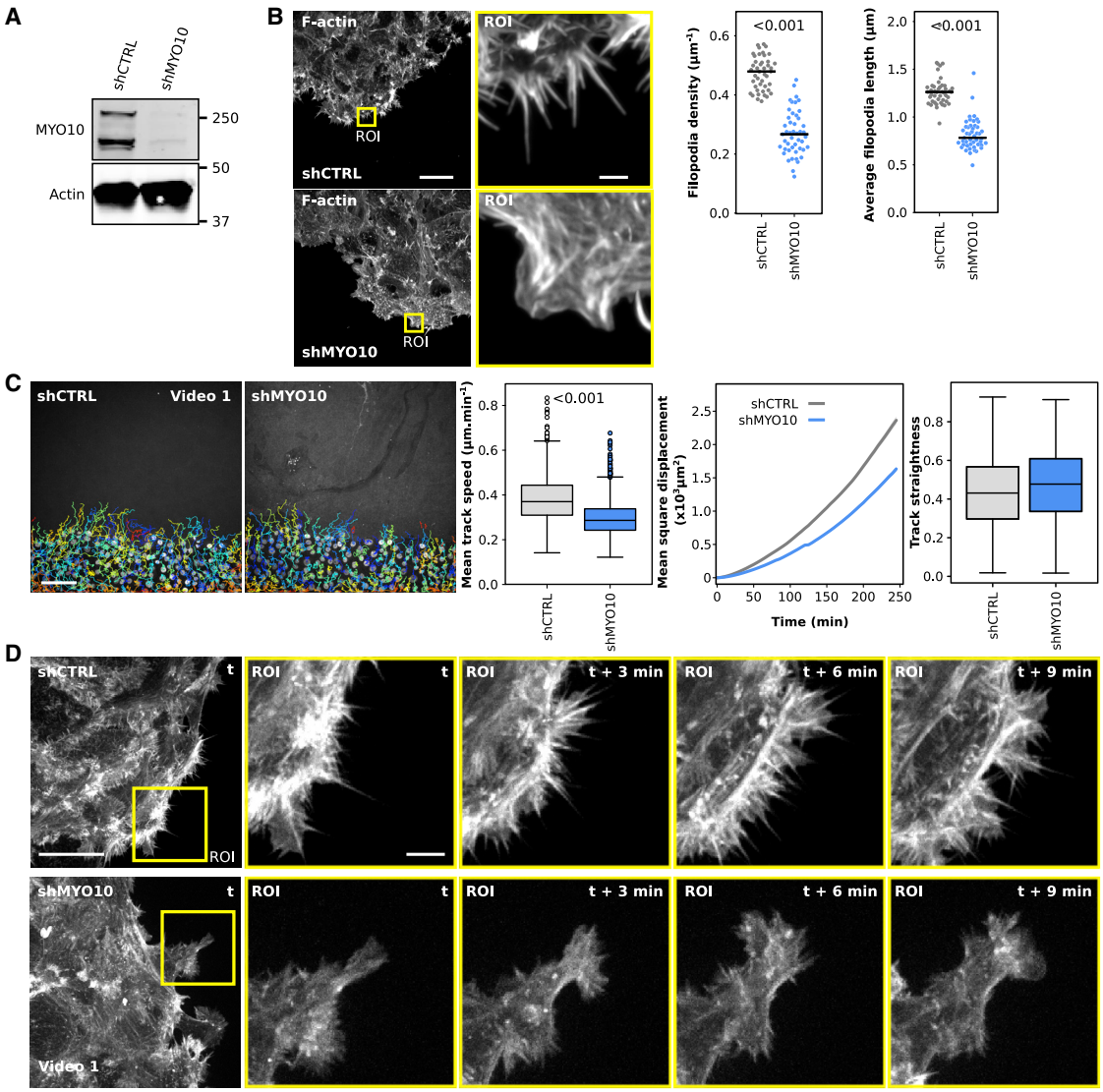

Figure 1. Filopodia depletion triggers a switch to lamellipodia-driven migration and limits cell motility

(A) shCTRL and shMYO10 DCIS.com cells were lysed, and MYO10 protein levels were analyzed by western blot.

(B) shCTRL and shMYO10 DCIS.com cells were left to migrate underneath a collagen gel for 2 days, fixed, stained, and imaged using a spinning-disk confocal microscope. A representative field of view (FOV) is displayed. Yellow squares highlight regions of interest (ROIs) that are magnified. Scale bars: (main) 25 µm and (inset) 2 µm. Filopodia density and the average filopodia length were analyzed using FiloQuant. Results are displayed as dot plots (n > 45 FOVs analyzed per condition; three independent experiments; randomization test).

(C) shCTRL and shMYO10 DCIS.com cells were left to migrate underneath a collagen gel for 1 day, incubated with SiR (silicon rhodamine)-DNA (to visualize nuclei), and imaged live using a spinning-disk confocal microscope (20× air objective). Cells were then automatically tracked using StarDist and TrackMate. A representative FOV with cell tracks is displayed. Mean track speed, mean square displacement, and track straightness were calculated using the motility lab website (three independent experiments, 30 FOVs per condition, and n > 2,300 cell tracks; randomization test). Scale bars: 100 µm.

(D) shCTRL and shMYO10 DCIS.com cells were left to migrate into a collagen gel for 1 day and imaged live using a spinning-disk confocal microscope (100× objective). A representative FOV with selected time points is displayed. Scale bars: (main) 25 µm and (inset) 5 µm.

See also Figure S1 and Video S1.

proteases that can degrade ECM molecules, releasing pro-invasive soluble cues and promoting the transition from *in situ* to invasive breast carcinoma (Ferrari et al., 2019; Lodillinsky et al., 2016; Monteiro et al., 2013). In addition, stromal cells may facilitate cancer-cell invasion by physically remodeling BMs (Glentis et al., 2017). To date, most of the research has focused on elucidating the mechanisms by which cancer cells breach established BMs. In contrast, very little is known about how cancer progression is coupled to general BM alterations and whether cancer cells themselves could contribute to BM assembly and maintenance.

Filopodia are small and dynamic finger-like actin-rich protrusions that interact with the ECM. Filopodia contain cell-surface receptors, such as integrins, cadherins, and growth factor receptors that can interact with and interpret a wide variety of cues (Fierro-González et al., 2013; Jacquemet et al., 2019; Valenzuela and Perez, 2020). Accordingly, filopodia are essential in guiding

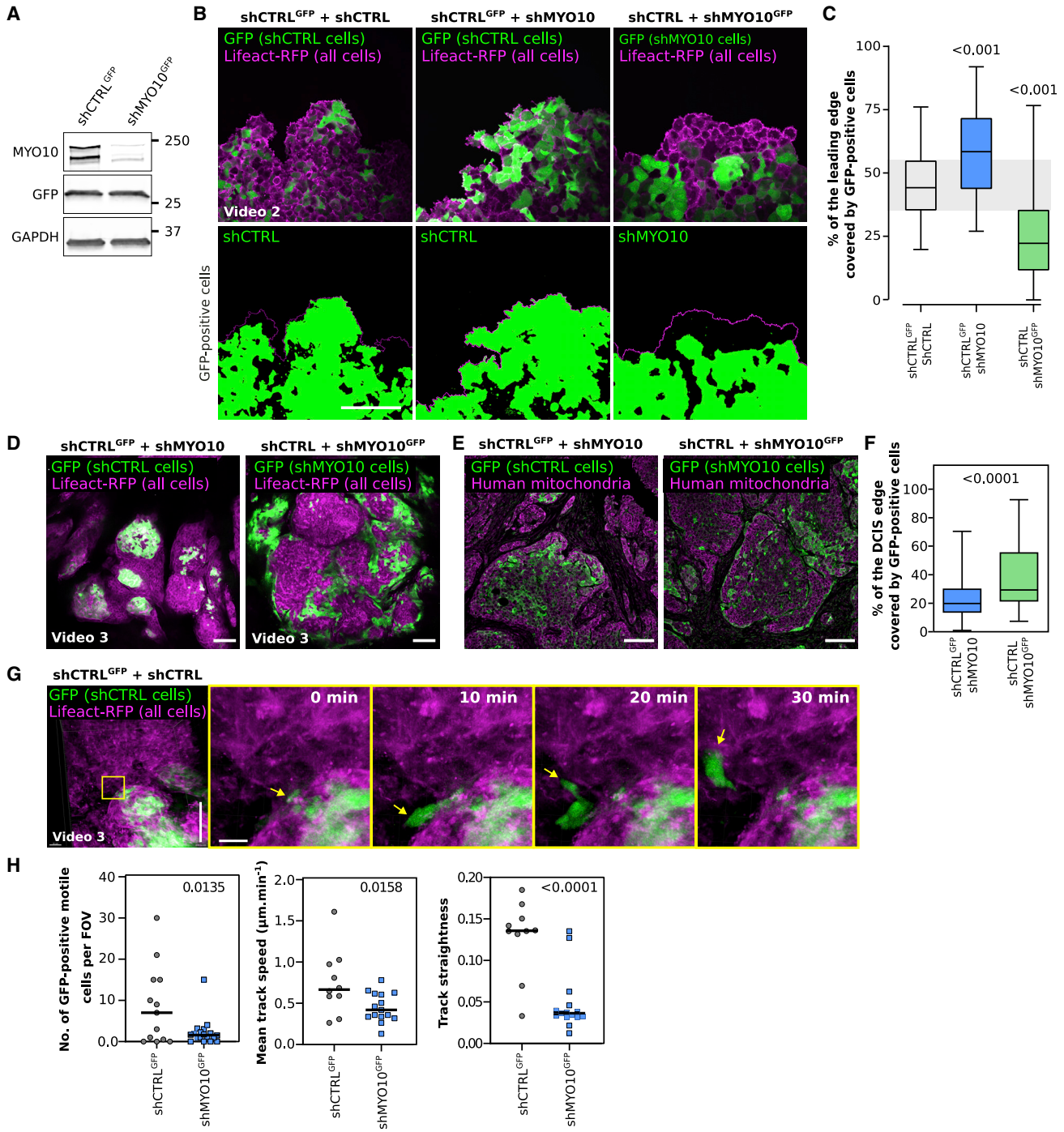

Figure 2. Cell competition experiments reveal that MYO10-filopodia contribute to the migratory behavior and multicellular organization of cancer cells *in vitro* and *in vivo*

(A) shCTRL and shMYO10 DCIS.com cells were infected with GFP-containing lentiviral particles, lysed, and analyzed for MYO10 and GFP expression levels. A representative western blot is displayed.

(B and C) GFP labeled or unlabeled shCTRL and shMYO10 DCIS.com cell lines were mixed in different combinations so that one of the cell lines was always GFP positive, and cell migration underneath a collagen gel was recorded live on a spinning-disk confocal microscope (20×). Representative images are displayed. Scale bars: 200 µm. The percentage of the leading edge covered by GFP-positive cells for each condition was measured using Fiji.

(C) The results are displayed as Tukey boxplots (n > 5,266 FOVs analyzed per condition; 3 biological repeats; *** p value < 0.001, randomization test).

(D–F) shCTRL^{GFP} + shMYO10 or shMYO10^{GFP} + shCTRL lifeact DCIS.com cells were xenografted in immunocompromised mice in a 1:1 ratio. The resulting xenografts were imaged by intravital tile scan imaging (25–35 days post-inoculation) (n = 2 tumors) (D) or dissected, sectioned, stained for human mitochondria, and imaged using a spinning-disk confocal microscope (20× objective) (25 days post-inoculation) (E). The percentage of the DCIS xenograft edge covered by

(legend continued on next page)

key cellular processes such as development, angiogenesis, immune surveillance, and wound healing (Jacquemet et al., 2015). Filopodia are also associated with increased invasion and metastasis in several cancer types and support cancer-cell survival at metastatic sites (Jacquemet et al., 2017; Shibue et al., 2012, 2013). Myosin-X (MYO10) is a well-established inducer of filopodia in many cell types and a positive regulator of migration and invasion of single and collectively migrating cells (Arjonen et al., 2014; Berg and Cheney, 2002; Summerbell et al., 2020). In IBC, MYO10 expression is upregulated by mutant p53, leads to metastasis, and correlates with poor patient outcomes (Arjonen et al., 2014; Cao et al., 2014).

To understand whether MYO10 filopodia contribute to the DCIS-to-IBC transition, we examined MYO10 expression in patient samples. MYO10 expression was increased in DCIS and IBC compared with the normal mammary epithelium. Rather surprisingly, the depletion of MYO10 expression intensified the loss of DCIS-like morphology in a xenograft model of breast cancer progression. It also induced an EMT (Epithelial to Mesenchymal transition)-like phenotype at the tumor borders and compromised BM formation around the DCIS lesions, leading to the dispersal of carcinoma cells into the surrounding stroma. Furthermore, imaging experiments demonstrated that MYO10-induced protrusions contribute to fibronectin assembly *in vitro*. Taken together, the data reported here support a model where MYO10 plays a dual role in breast cancer. At the DCIS stage, MYO10 expression supports the generation of a tumor-stroma barrier, whereas, at the IBC stage, MYO10 induces cancer-cell migration and dissemination.

RESULTS

MYO10-filopodia depletion limits collective cell migration *in vitro* and individual cancer-cell motility *in vivo*

The evolution of cancer is frequently modeled using related cell lines with progressing malignancy. One such model is the widely used immortalized breast epithelial cells (MCF10A), their H-Ras transformed variants (MCF10AT cell line) that are tumorigenic as xenografts, and the tumorigenic and invasive cells derived from MCF10AT (MCF10DCIS.com cell line; Dawson et al., 1996; Miller et al., 2000). Xenografts of the MCF10DCIS.com cells recapitulate DCIS disease progression, from early stages of tumor formation to invasive carcinoma, mimicking the human disease (Miller et al., 2000; Behbod et al., 2009; Lodillinsky et al., 2016) (Figure S1A). Previously, we have shown that MCF10DCIS.com cells (called DCIS.com cells here for simplicity) display high numbers of filopodia as they invade collectively *in vitro* (Jacquemet et al., 2017). However, the role of MYO10 in these cells remains unknown. To investigate MYO10 dependency in generating these filopodia, we silenced MYO10 expression using two independent short hairpin RNA (shRNA) oligos. Both shRNAs silenced MYO10 efficiently and reduced filopodia density similarly (Figures S1B–S1D). Subsequently, we pooled four MYO10-depleted single-cell clones to create the stable shMYO10 DCIS.com cell line used in this study (Figures 1A, S1E, and S1F). Silencing of MYO10 led to a marked reduction in filopodia density and length in cells migrating in 2D (Figure 1B) and decreased cell invasion speed through collagen in a 2D overlay assay (Figure 1C; Video S1). Furthermore, high-resolution live-cell imaging revealed that in the absence of filopodia, shMYO10 DCIS.com cells switch to a lamellipodia-driven mode of collective cell migration (Figure 1D; Video S1). Taken together, these data indicate that MYO10 regulates the protrusive activity and collective migration of DCIS.com cells *in vitro*.

MYO10-filopodia contribute to the multicellular organization of cancer cells *in vitro* and *in vivo*

To study the role of MYO10 filopodia in organizing cells within a monolayer, we mixed shCTRL and shMYO10 cells (alternating GFP labeling of the cell lines) (Figure 2A) and recorded cell migration live (Figure 2B; Video S2). Notably, shMYO10 cells consistently lagged behind shCTRL cells, which preferentially localized to the front of the collectively migrating cells (Figures 2B and 2C; Video S2). This result demonstrates that MYO10 expression segregates cancer cells within an actively migrating monolayer.

Cell migration also contributes to tumor multicellular organization (Waclaw et al., 2015). To investigate whether filopodia would also contribute to the cellular localization pattern in DCIS-like tumors *in vivo*, we used two-photon intravital microscopy (Figures 2D and S2) and tumor histology (Figure 2E). We examined the localization of shCTRL and shMYO10 cells within the same tumor (mice were grafted with a 50:50 mixture of shCTRL and shMYO10 cells with GFP expressed in either shCTRL or shMYO10 cells). The tumor boundary was defined by IHC labeling mitochondria with a human-specific antibody. We observed an obvious preferential segregation of shMYO10 cells to the edges of the tumor acini while shCTRL cells tended to accumulate toward the center (Figures 2D–2F; Video S3). This result indicates that MYO10 can also contribute to the multicellular organization of tumor cells *in vivo*. Surprisingly, the segregation of MYO10-depleted cells was inverted compared with the *in vitro* freely migrating setup described above (Figures 2B and 2C). These data indicate that MYO10 may contribute to distinct cell behavior in pre-invasive confined tumors and actively migratory tumor cells.

Despite the preferential recruitment of MYO10-depleted cells at the edges of tumor acini, GFP-based single-cell tracking from live two-photon intravital imaging (Figure 2G) indicated that shCTRL cells had increased single-cell migration out of the DCIS-like acini *in vivo* compared with shMYO10 cells (Figure 2H; Video S3). This result agrees with our *in vitro* migration experiments indicating that MYO10 depletion reduces cell migration (Figure 1C). Thus, MYO10 filopodia contribute to the migratory behavior and the multicellular organization of cancer cells *in vitro* and *in vivo*.

GFP-positive cells was then scored using Fiji. The results are displayed as Tukey boxplots (F) (n = 4 tumors per condition; FOVs analyzed: shCTRL^{GFP} + shMYO10, 114; shMYO10^{GFP} + shCTRL, 103; Mann-Whitney test). Scale bars: 100 μm.
(G and H) shCTRL^{GFP} or shMYO10^{GFP} DCIS.com cells were injected in combination with non-GFP-labeled cells in immunocompromised mice. Intravital imaging of tumors was conducted 25–35 days post-inoculation. Representative images for the shCTRL^{GFP} + shCTRL (non-GFP) are displayed (G). Yellow inset is a ROI that is magnified over the video timeline. Scale bars: (main) 100 μm and (inset) 15 μm. All visibly motile GFP-positive cells were tracked manually in three dimensions using the Imaris software, and the number of motile cells per FOV, and mean track speed and track straightness (displacement/length of track) per cell were quantified (n = 4 shCTRL^{GFP} tumors with 2–4 FOVs per tumor; and n = 6 shMYO10^{GFP} tumors with 1–5 FOVs per tumor; Student's t test) (H). FOV, field of view.
See also Figure S2 and Videos S2 and S3.

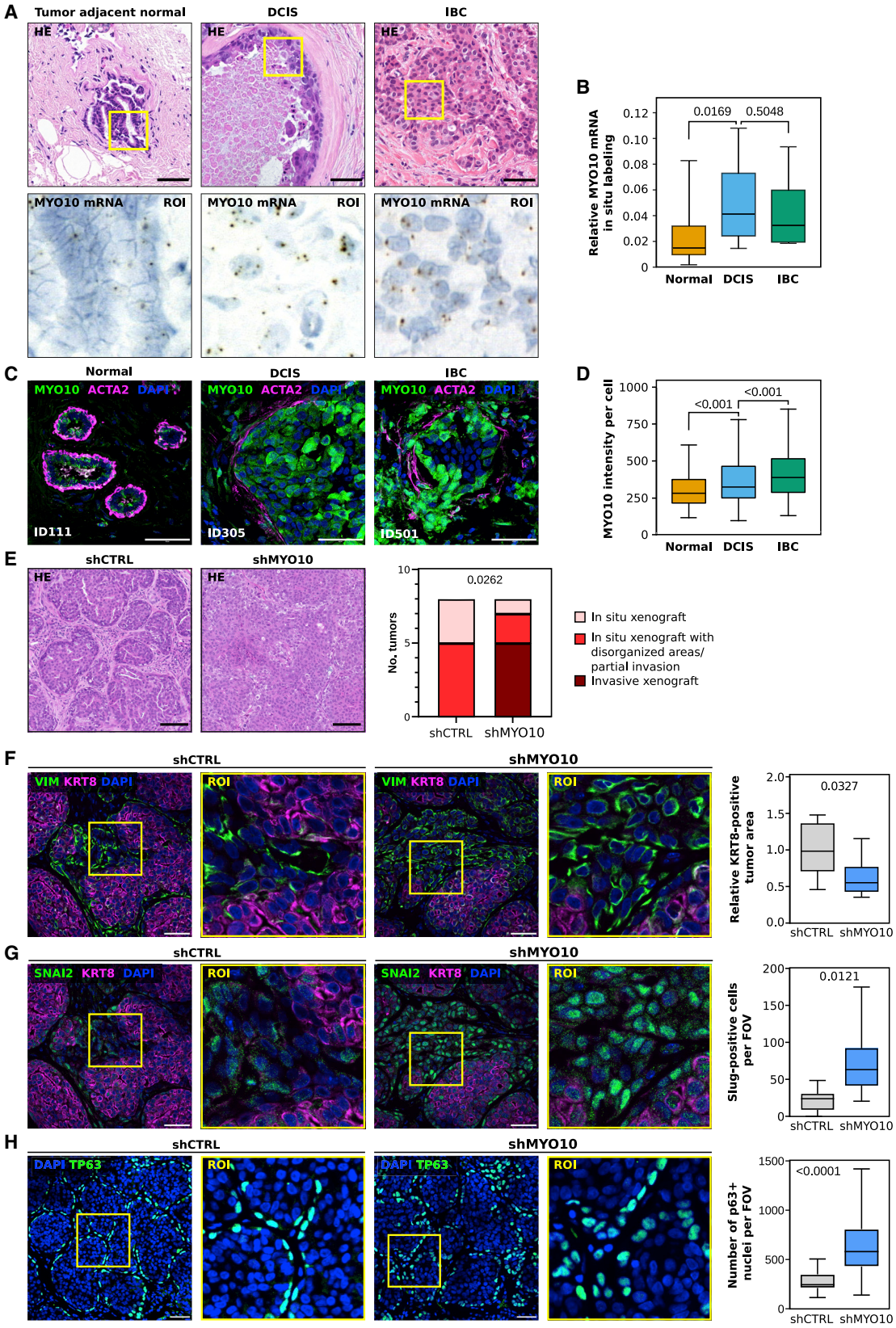

(legend on next page)

MYO10 expression is elevated in human breast carcinoma, and MYO10 depletion induces cancer-cell dispersal and EMT *in vivo*, specifically at the tumor border

MYO10 is highly expressed in a subset of breast carcinomas with poor prognosis (Arjonen et al., 2014). However, MYO10 expression at the early, non-invasive stage of breast cancer has not been investigated. We obtained freshly excised tissues from a set of patients diagnosed with DCIS or with IBC (Figure S3A). MYO10 mRNA expression was first detected using RNA *in situ* hybridization. The DCIS lesions had a broad distribution of MYO10 expression levels (Figures 3A, 3B, S3B, and S3C), and MYO10 mRNA was observed both at the center and the edges of the DCIS acini (Figures S4A and S4B). Importantly, the average MYO10 mRNA expression was significantly higher in DCIS lesions than in the histologically normal regions of the mammary epithelial tissue but was comparable between DCIS and IBC samples (Figures 3A, 3B, S3B, and S3C). Further analysis of MYO10 expression at the protein level (immunostaining of frozen tissue sections) revealed dramatic intra-tumor heterogeneity in both DCIS and IBC tumors (Figures 3C and 3D). Cells with high MYO10 protein levels were detected both inside and at the edges of tumors and were more numerous in invasive samples. Accordingly, the overall staining intensity was significantly higher in IBC compared with DCIS tumors (Figures 3C and 3D), in line with earlier reports indicating that high MYO10 expression correlates with poor patient outcomes in breast cancer (Arjonen et al., 2014; Cao et al., 2014).

To determine whether MYO10 also plays a role during the early stages of tumor progression, we used the DCIS-like tumor xenografts that transition from DCIS to IBC over time *in vivo* (Figure S1A). Using this tumor model, we observed a modest decrease in overall MYO10 mRNA expression level. However, when comparing the intra-tumor localization of the MYO10 mRNA, we detected a significant increase in MYO10 expression, specifically at the invasive xenograft edges during tumor progression (Figures S4C–S4E). To test the outcome of MYO10 depletion *in vivo*, we generated shCTRL and shMYO10 xenografts. MYO10 silencing did not affect cell growth in 2D culture (Figure S5A), and shCTRL and shMYO10 xenograft tumor sizes were comparable (Figures S5B and S5C). Next, we compared the onset of invasion in shCTRL and shMYO10 xenografts by blind scoring the degree of invasion based on tumor histology (Figures 3E and S5D). As expected, at 25 days post-inoculation, shCTRL tumors were composed of DCIS-like acini or acini exhibiting partial invasion (Figure 3E). In contrast, most shMYO10 tumors displayed partial or complete invasion and loss of the *in situ* tumor organization (Figure 3E).

Breast cancer is a heterogeneous disease and presents with a varying degree of EMT that has been associated with increased tumor invasion. Immunostaining of the xenografts with markers for epithelial/luminal-like (keratin 8; KRT8) and mesenchymal/basal-like breast cancer cells (vimentin [VIM, human-specific antibody] and the transcription factor Slug [SNAI2]) revealed a notable presence of cancer cells with mesenchymal traits, particularly at the perimeter of MYO10-depleted xenografts (Figures 3F and 3G). Additional basal myoepithelial markers p63 (TP63), α6 integrin (ITGA6), and α smooth muscle actin (αSMA/ACTA2), clearly expressed at the edges of all tumors, further validated the observation that basal-like cells were distributed over a broader margin at the border of shMYO10 tumor acini (Figures 3H, S5E, and S5F). Thus, MYO10 depletion leads to an increased presence of tumor cells with mesenchymal/basal-like features that may be the cause or the consequence of the faster onset of tumor invasion in MYO10-depleted tumors.

MYO10 depletion leads to defective basement membranes *in vivo*

Breaching the BM barrier is a critical step in the DCIS transition to IBC. To visualize possible BM alterations, we stained for BM components in the tumor xenografts (Figure 4A). 25-day-old tumors formed by shCTRL cells were surrounded by a clear, seemingly continuous collagen IV and laminin-positive BM. In contrast, the BM around shMYO10 tumors was harder to detect with decreased collagen IV and laminin staining (Figures 4A and 4B). BMs contribute to the assembly of other ECM scaffolds, including the proper assembly of fibronectin fibrils (Lu et al., 2020). In line with this notion, we observed that the fibronectin matrices in shMYO10 tumors were less developed, and the ECM surrounding the tumors contained less fibronectin than the shCTRL tumors (Figures 4A and 4B).

A similar defect in collagen IV deposition around shMYO10 acini was apparent at an earlier stage of tumor development when acini initially formed (10 days post-inoculation) (Figure 4C). Although fibronectin staining intensity appeared equal in shCTRL and shMYO10 tumors, visible fibronectin fibrils, constituting a continuous network, were mostly absent in shMYO10 acini. Instead, bright fibronectin puncta, which are reminiscent of folded fibronectin not yet assembled into filaments, could be observed at the edges of shMYO10 acini (Figures 4A, S6A, and S6B).

The lack of BM assembly in the MYO10-depleted tumors was also observed with electron microscopy (EM). In negatively stained EM, BMs were visible (as dark fibers) at the edges of shCTRL acini but could not be easily observed in shMYO10 tumors (Figure 4D).

Figure 3. MYO10 expression is elevated in human breast carcinoma, and MYO10 depletion induces cancer-cell dispersal and EMT *in vivo*, specifically at the tumor border

(A and B) *In situ* labeling of MYO10 mRNA in human breast samples. (A) Representative images of histology (HE) and MYO10 mRNA (brown dots) in normal breast epithelial regions (n = 6), ductal carcinoma *in situ* (DCIS, n = 4), and invasive breast carcinoma (IBC, n = 2). Magnified images of the corresponding regions are shown in ROI. Scale bars: 50 μm. (B) Quantification of the MYO10 mRNA spot area relative to the nuclear area (normal = 16; DCIS = 14, IBC = 10 FOVs, Student's t test).
(C and D) MYO10 protein levels were analyzed in healthy breast (n = 3), DCIS (n = 3), and IBC (n = 2) frozen tissue sections by immunolabeling along with myoepithelial (ACTA2) and nuclear labeling (DAPI). The fluorescence intensity of MYO10 immunolabeling was quantified per epithelial/tumor cell (normal = 3,700; DCIS = 3,546, IBC = 1,416 cells; randomization test). Scale bars: 50 μm.
(E–H) shCTRL and shMYO10 cells were injected subcutaneously in NOD.scid mice. At 25 days post-inoculation, tumors were dissected, and tissue sections were labeled as indicated. Representative images of tumor histology (HE) and quantification of invasiveness are shown (n = 8 tumors, chi-square test) (E). Representative images of day 25 tumor sections labeled for vimentin (human-specific antibody, VIM) (F), or slug (SNAI2) (G) with keratin-8 (KRT8), or the myoepithelial marker p63 (TP63) (H) were taken using a confocal microscope. The relative area of the KRT8-positive tumor (F) and the average number of slug-positive cells (G) or p63-positive nuclei per FOV (H) were quantified (G, n = 8 tumors; Student's t test; H, n = 24 FOVs from 5 tumors per genotype). Scale bars: 50 μm.
See also Figures S3–S5.

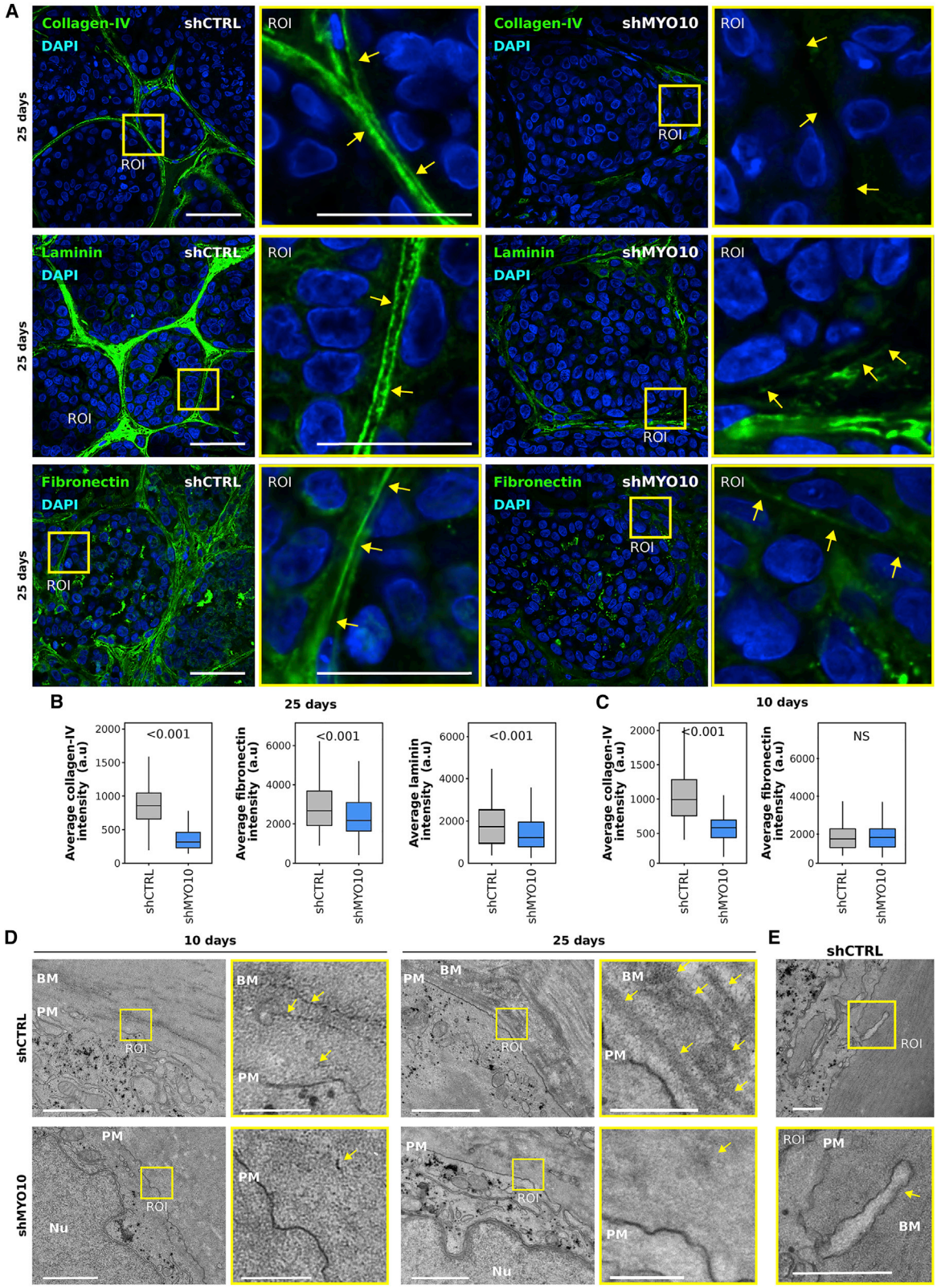

Figure 4. MYO10 loss leads to defective basement membranes *in vivo*

(A–C) Tissue section of shCTRL and shMYO10 DCIS-like xenografts at 25 days (A and B) and 10 days post-inoculation (C) were labeled for DAPI and collagen IV, fibronectin, or laminin and imaged using a spinning-disk confocal microscope (63× objective). Representative FOVs of day 25 DCIS-like xenografts are displayed. Scale bars: (main) 50 μm and (inset) 25 μm (A). The average integrated density of collagen IV, fibronectin, or laminin labeling around the DCIS acini was measured using

(legend continued on next page)

Moreover, occasional filopodia-like protrusions were observed at the edge of the shCTRL, but not shMYO10 DCIS-like xenografts (Figure 4E). Taken together, these data indicate that the BM of shMYO10 acini is compromised *in vivo* at different stages of tumor progression and point to inadequate BM production or assembly rather than degradation, which typically occurs at a much later stage in tumor progression (Lodillinsky et al., 2016).

ECM expression is upregulated in MYO10-depleted tumors

The tumor microenvironment comprises ECM generated by stromal and tumor cells. However, in human clinical samples or genetically engineered mouse tumor models, the distinction between the ECM-producing cells is complicated. We took advantage of our ability to distinguish gene expression changes in the tumor (human genes) and the stroma (mouse genes) in our model system and performed mRNA sequencing of shCTRL and shMYO10 tumors (at 25 days post-inoculation) to investigate the expression of BM components. MYO10 expression was decreased in shMYO10 tumors, validating our approach (Figure S6C). Overall, stromal gene expression profiles were nearly identical in shCTRL and shMYO10 tumors (Figure 5A; Table S1). In contrast, tumor gene expression profiles were distinct, with many differentially expressed genes detected between the shCTRL and shMYO10 DCIS samples (Figure 5B; Table S1). Of note, the expression of the filopodia-inducing proteins FMNL3 and neurofascin were increased in shMYO10 tumors, indicating a possible compensatory mechanism to promote filopodia formation when MYO10 is downregulated (Figures S6D and S6E).

Expression of several ECM molecules, including collagen IV (COL4A1, COL4A2, COL4A5, and COL4A6), collagen VI (COL6A1), laminin (LAMA1), and fibronectin (FN1), were increased at the mRNA level in shMYO10 tumors (Figures 5C and S6C), which was unexpected considering the inadequate BM generation in these tumors (Figure 4). Furthermore, gene ontology analyses and annotation of our dataset using the Matrisome database (Naba et al., 2012, 2016, 2017) confirmed that MYO10-depleted xenografts express ECM genes more overall (Figures 5D and 5E). *In vitro*, we found that MYO10-depleted cells had elevated fibronectin and collagen IV protein levels compared with shCTRL cells (Figure 5F). Taken together, these data indicate that the tumor cells are a significant source of the BM components in these DCIS-like tumors and that MYO10 depletion does not reduce BM component production but instead leads to an overall increase in ECM production *in vivo*.

MYO10-filopodia engage and contribute to fibronectin assembly in 3D

Previous work indicates that 3D matrigel-embedded non-transformed mammary epithelial spheroids assemble BM (Wang et al., 2013). To assess whether tumor-cell filopodia contribute to ECM assembly, we set up 3D spheroid assays, reconstituting BM component assembly *in vitro*. We incubated DCIS.com spheroids with fluorescently labeled ECM molecules and observed an apparent layer of labeled fibronectin and laminin around the spheroids and ECM proteins in close vicinity of filopodia tips (Figures 6A, 6B, S7A, and S7B). Filopodia tethering of labeled fibronectin fibers was also detected when imaging spheroids live, indicating that this is an active process and not a fixation artifact (Video S4). Filopodia tips have small integrin-containing adhesions, which interact with the ECM to facilitate filopodia stability (Jacquemet et al., 2016; Miihkinen et al., 2021). We cannot definitively conclude whether the spheroids' filopodia in our set-up bind to the ECM. However, the presence of active β1-integrin at filopodia tips would strongly support this possibility (Figures 6C and 6D).

Downstream of integrins, MYO10-filopodia are dependent on Src-kinase activity, whereas inhibition of cell body contractility with the myosin-II inhibitor blebbistatin triggers elongation of filopodia (Jacquemet et al., 2016; Stubb et al., 2020). Inhibiting a subfamily of integrins with an integrin β1 blocking antibody (AIIB2) significantly reduced fibronectin recruitment to spheroids (Figures 6E–6G). The effect of Src inhibition was even more pronounced, resulting in a weaker fibronectin signal around the spheroids and displacement of the signal to the spheroid interior (Figures 6E–6G; Video S5). The ECM barrier became discontinuous in both cases compared with the fibronectin ECM recruited by control-treated spheroids (Figures 6E–6G). In stark contrast, blebbistatin triggered a prominent invasion of collective, filopodia-rich cell strands from the spheroids (Figure 6E). The ECM barrier around the non-invading areas of the spheroids appeared intact but was clearly displaced at the invasive areas (Figure 6E).

Finally, we performed the same ECM assembly assay in MYO10-depleted spheroids. In line with the previous results, we observed that MYO10 silencing decreased filopodia density and resulted in a much weaker accumulation of fibronectin around the spheroids (Figures 7A and 7B), indicating that MYO10-induced filopodia contribute to fibronectin assembly in 3D. Somewhat unexpectedly, laminin-111 recruitment to the spheroids was not affected by the inhibitors or MYO10-depletion (Figures S7C–S7F). This implies that our 3D BM assembly assays do not fully recapitulate the features of BM generation *in vivo*, perhaps due to the high abundance of unlabeled laminin in Matrigel, in which the spheres are embedded. Altogether, these 3D ECM recruitment assays suggest a functional role for MYO10-filopodia in fibronectin assembly *in vitro*.

MYO10 promotes pseudopod-like protrusions at the tumor edges *ex vivo*

Intrigued by the putative functional role of MYO10-dependent protrusions in ECM assembly, we turned to live *ex vivo* imaging of

Fiji. The results are displayed as boxplots (B and C) (day 25 xenografts, n > 233 DCIS acini from 5 tumors per condition; day 10 xenografts, n > 32 DCIS acini from 4 tumors per condition; randomization test).

(D) Day 10 and day 25 shCTRL and shMYO10 DCIS-like xenografts were imaged using electron microscopy to visualize the BM surrounding the DCIS acini. Representative FOVs are displayed (25 days xenografts, three biological repeats; 10 days xenografts, four biological repeats). Scale bars: (main) 1 μm and (inset) 250 nm.

(E) Day 25 shCTRL DCIS-like xenografts were imaged using electron microscopy to visualize the protrusions surrounding the DCIS acini. Scale bars: (main) 500 nm; (inset) 500 nm. For all panels, p values were determined using a randomization test. NS indicates no statistical difference between the mean values of the highlighted condition and the control. PM, plasma membrane; Nu, nucleus; BM, basement membrane.

See also Figure S6.

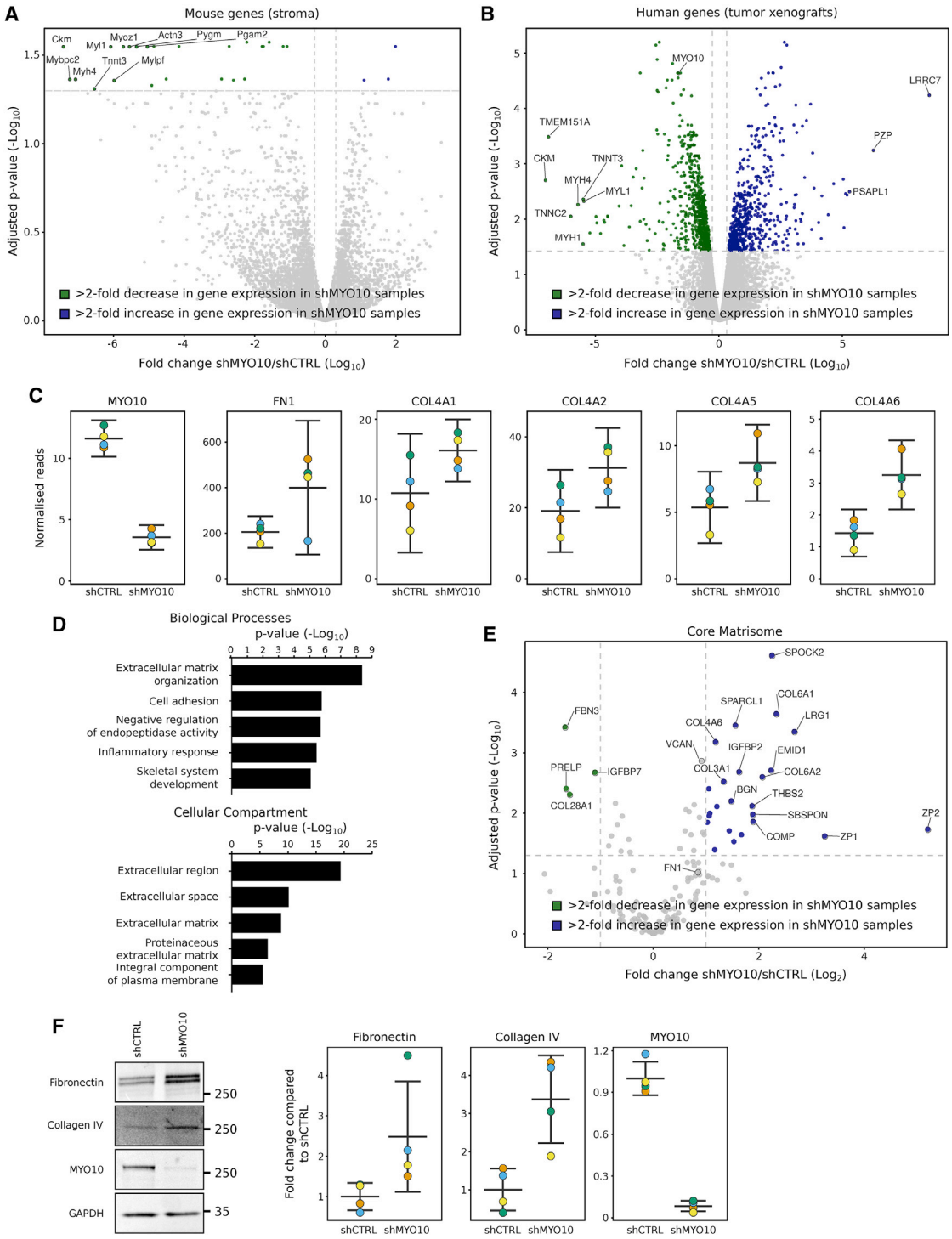

Figure 5. MYO10 depletion drives the expression of ECM genes by cancer cells

(A–E) 25-day-old shCTRL and shMYO10 DCIS-like xenografts were dissected and their RNA sequenced. The expression levels of the mouse genes (tumor stroma) and of the human genes (tumor) were analyzed separately (Table S1, see STAR Methods for details, four different mice per condition). The overall gene expression changes in the stroma (A) or the tumors (B) upon MYO10 silencing are displayed as volcano plots. Genes with at least a 2-fold increase in their expression levels upon MYO10 silencing are highlighted in blue, whereas genes with at least a 2-fold decrease in their expression levels upon MYO10 silencing are highlighted in green. The most affected genes and MYO10 are annotated (B). The expression levels of MYO10 and selected ECM genes FN1, COL4A1, COL4A2, COL4A5, and COL4A6 in 25-day-old shCTRL and shMYO10 DCIS-like xenografts were measured by RNA-seq and displayed as SuperPlots (C). Gene ontology-based functional annotation analyses of human genes overexpressed in shMYO10 tumors (biological process and cellular compartment) were

(legend continued on next page)

ECM-embedded tumors. Day 25 DCIS.com xenografts were dissected, embedded in a collagen gel, and imaged at high resolution. We observed cells at the border of *in situ* tumor acini extending large protrusions that interacted with the surrounding ECM (Figures 7C and 7D; Video S6). Notably, although very frequent in shCTRL cells, these protrusions were primarily absent in shMYO10 xenografts (Figures 7E and 7F; Video S6). These data indicate that MYO10 contributes to the generation of ECM-probing protrusions at the tumor border, reminiscent of the protruding filopodia detected in the 3D spheroids (Figures 7A and 7B). Although these protrusions are much bigger than individual filopodia and instead resemble pseudopods, we anticipate that these structures are linked to the ability of the DCIS xenografts to self-assemble the tumor surrounding BM, which is defective in the shMYO10 tumors lacking these dynamic protrusions. Altogether, our data indicate that MYO10 contributes to the protrusive activity of DCIS.com cells *in vivo* in tumor xenografts. These protrusions are essential for proper BM assembly, limiting the DCIS-to-IBC transition. In contrast, silencing of MYO10 correlates with defects in BM assembly *in vivo* and *in vitro*, facilitating a transition from DCIS to IBC.

DISCUSSION

An increasing number of studies indicate a pro-invasive role for MYO10-induced filopodia in aggressive human cancers ranging from lung cancer to melanoma (Arjonen et al., 2014; Cao et al., 2014; Summerbell et al., 2020; Tokuo et al., 2018). Here, we set out to study the role of MYO10 at an earlier stage of breast cancer, in premalignant *in situ* tumors, and during the transition to invasive carcinoma. Our observations support a model in which MYO10 plays a dual role in breast cancer progression. In early-stage disease, MYO10 expression correlates with the presence of a BM barrier confining DCIS-like tumors. However, in IBC, MYO10 filopodia are pro-invasive and contribute to metastasis in mouse models and correlate with poor disease outcomes in patients (Arjonen et al., 2014; Cao et al., 2014).

Using high-resolution imaging of 3D spheroids, we observed that fibronectin is recruited by filopodia and deposited around the spheres. This is consistent with a growing body of evidence for filopodia-like protrusions directly contributing to ECM remodeling (Malandrino et al., 2019; Sato et al., 2017; Summerbell et al., 2020). Although the precise mechanism(s) by which filopodia remodel ECM remains to be determined, filopodia can assemble adhesive structures capable of interacting with different ECM molecules (Albuschies and Vogel, 2013; Jacquemet et al., 2019; Miihkinen et al., 2021). Filopodia can also exert forces on the underlying substrate, contributing to the remodeling process (Bornschlögl et al., 2013; Brockman et al., 2020; Cojoc et al., 2007; Leijnse et al., 2015). This might explain how filopodia-like protrusions can remodel fibronectin (Sato et al., 2017; Summerbell et al., 2020), a process known to require mechanical input from cells (Singh et al., 2010). We observe that laminin assembly in the spheroid model is not dependent on MYO10-filopodia. This is likely due to limitations with the *in vitro* model to fully recapitulate the features of *in vivo* BMs. It could also be linked to the fact that BMs have been proposed to self-assemble independently of forces and integrins (Jayadev and Sherwood, 2017). However, further studies are necessary to uncover how filopodia protrusions promote BM assembly *in vivo* during DCIS progression. Taken together, our data are compatible with two scenarios; either MYO10-deficient cells become more invasive due to defective BM deposition or cells gain invasive capacity and consequently deposit less matrix. Finally, the contribution of MYO10 filopodia to BM assemby/remodeling in other biological contexts remains to be established.

To invade the surrounding tissues, tumor cells generally need to cross the BM. In this context, BMs are typically viewed as stable barriers that inhibit cancer dissemination. However, recent evidence also suggests that BMs can be very dynamic structures that undergo fast and constant remodeling (Keeley et al., 2020). Although, to the best of our knowledge, BM turnover has yet to be observed in tumors, the results presented here would support a model whereby cancer cells contribute to the production and assembly of the ECM. Previous work, using proteomic studies, concluded that cancer cells produce a significant fraction of the ECM in the breast tumor stroma (Kozma et al., 2021; Naba et al., 2014; Sflomos et al., 2021). Interestingly, tumors lacking MYO10 had not only deficient BM but also higher ECM gene expression. Therefore, it is tempting to speculate that compensatory mechanisms favor ECM production when ECM assembly is deficient.

DCIS diagnosis is not life-threatening but becomes potentially lethal in patients who progress to IBC. Therefore, understanding the molecular mechanisms of DCIS-to-IBC transition is of clinical importance. A recent study compared the DCIS epithelium and its microenvironment in patients with or without subsequent invasive relapse (Risom et al., 2022). Their data indicated that patients with increased stromal cell infiltration, desmoplasia, and ECM remodeling were less likely to relapse to invasive disease (Risom et al., 2022). This study brings forward the intriguing notion of increased stromal desmoplasia correlating with a good prognosis in DCIS, contrary to its widely accepted role in tissue stiffening and cancer progression in IBC (Piersma et al., 2020; Schedin and Keely, 2011). Our data indicate that DCIS tumors with reduced BM enwrapping are increasingly invasive. This may, at first, seem contradictory to the recent Risom et al. study. However, the exact composition of the tumor proximal ECM is most likely critical, and BM and desmoplastic ECM are structurally and biochemically different. Therefore, tumors enwrapped by a BM will progress differently from tumors lacking a BM regardless of the presence or absence of a desmoplastic tumor microenvironment.

MYO10 is frequently overexpressed in breast cancer, where its expression is induced by mutant p53 and correlates with poor prognosis (Arjonen et al., 2014; Cao et al., 2014). MYO10 silencing decreases cancer-cell invasion and metastasis of aggressive breast cancer cells *in vitro* and *in vivo* (Arjonen et al., 2014), and MYO10 contributes to the invasion of other aggressive cancers, including melanoma and glioblastoma (Kenchappa et al., 2020;

performed using DAVID (Huang et al., 2009). The top five categories (based on their adjusted p values) are displayed (D). Volcano plots highlighting the changes in core Matrisome gene expression upon MYO10 silencing (as defined by the Matrisome project, http://matrisomeproject.mit.edu/) (E).
(F) The expression level of multiple proteins (as indicated) was measured in shCTRL and shMYO10 cell lysates using western blots (n = 4 independent repeats). For all panels, the results are displayed as SuperPlots (Goedhart, 2021; Lord et al., 2020).
See also Figure S6.

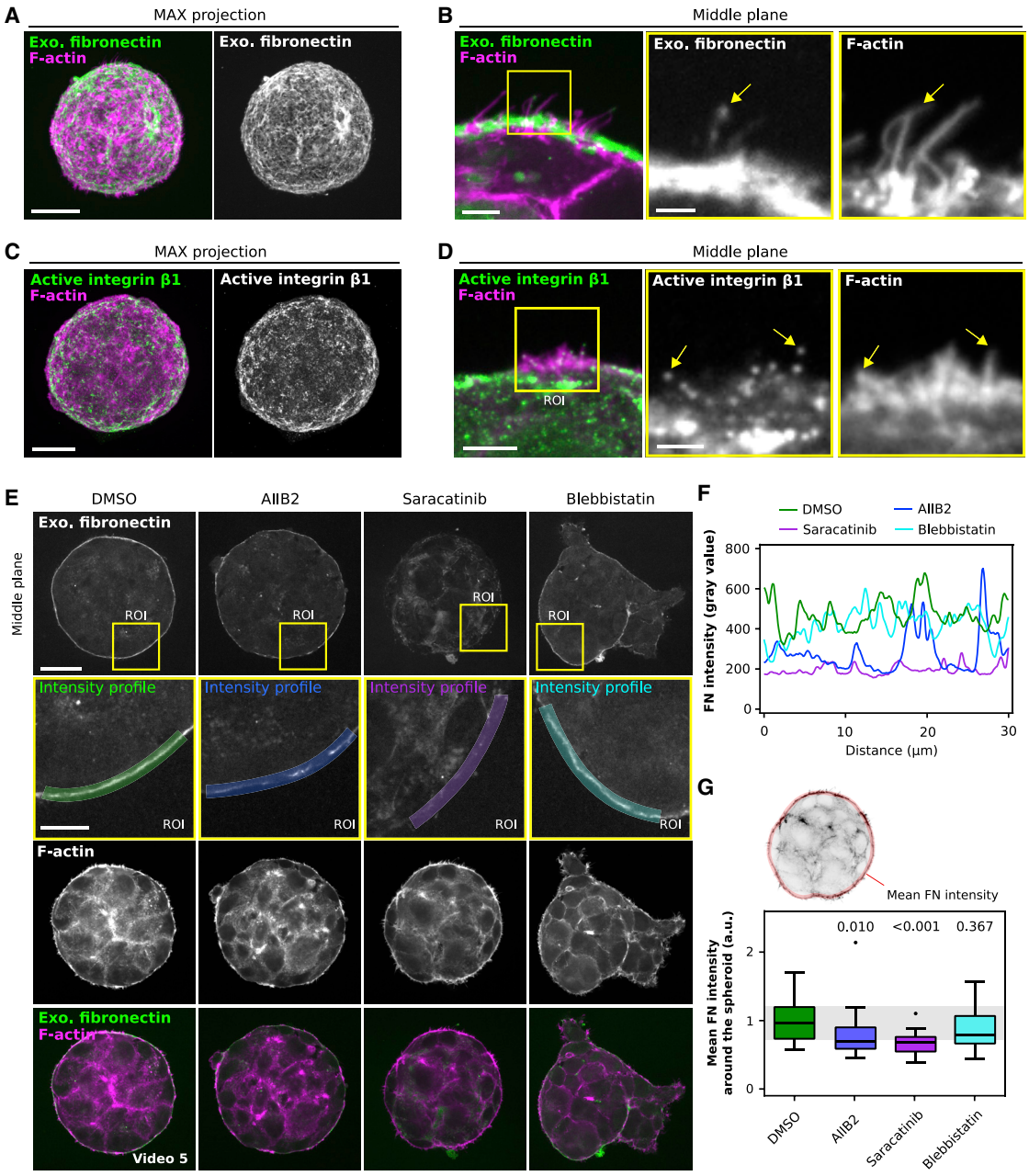

Figure 6. Filopodia engage ECM components in 3D

(A–D) Lifeact-mRFP-expressing DCIS.com cells were seeded as single cells in Matrigel and were allowed to form spheroids for 3 days. The spheroids were either incubated with fluorescently labeled fibronectin 24 h before fixation (A and B) or stained for active β1-integrin (monoclonal antibody 9EG7) after fixation and imaged using a spinning-disk confocal microscope (C and D). Representative FOVs highlighting maximum intensity projections (A and C) and the spheroids' edges are displayed (B and D). (A and C) Scale bars: 20 μm. (B and D) Scale bars: (main) 5 μm and (inset) 2 μm.

(E and F) Fluorescence images (E) and intensity profiles (F) depicting the accumulation of exogenous (exo.) fibronectin on spheroids treated with integrin/actomyosin-targeting compounds. Lifeact-mRFP-expressing DCIS.com cells were allowed to form spheroids for 2 days before the cultures were supplemented with fluorescently labeled fibronectin and either DMSO, blebbistatin, integrin β1-blocking antibody (AIIB2), or saracatinib. After an overnight treatment, the samples were fixed and imaged using a spinning-disk confocal microscope. Scale bars: (main) 30 μm and (inset) 10 μm.

(G) Mean fibronectin intensity around each spheroid. Results are displayed as Tukey boxplots (n = 23–32 spheroids; 2 biological repeats; Kruskal-Wallis one-way ANOVA with Dunn's post hoc test).

See also Figure S7 and Videos S4 and S5.

Tokuo et al., 2018). In line with these previous studies, we found that targeting MYO10 expression leads to reduced cell migration *in vitro* and *in vivo*. However, our results also imply that MYO10 plays a dual role in breast cancer progression with a protective, BM-supportive function in early-stage disease. Although we could not address the metastatic progression in the DCIS xenograft

CellPress
OPEN ACCESS

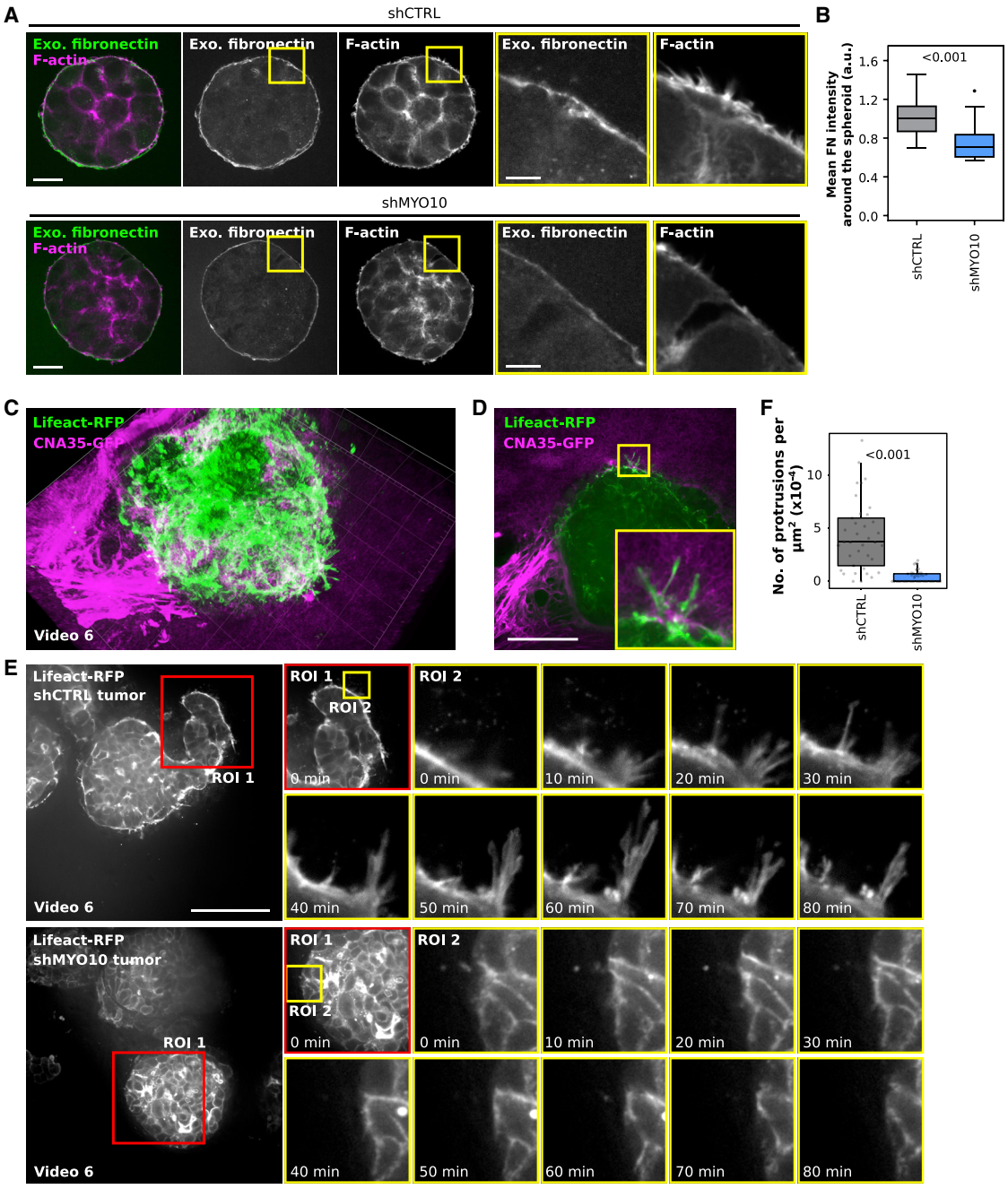

Figure 7. MYO10 modulates fibronectin assembly *in vitro* and cell protrusions at the tumor boundary *ex vivo*

(A and B) shCTRL and shMYO10 DCIS.com cells were allowed to form spheroids as in (Figure 6) in the presence of fluorescently labeled fibronectin and imaged using a spinning-disk confocal microscope (63× objective). Representative FOVs highlighting the spheroids' middle planes are shown. Scale bars: (main) 20 μm and (inset) 5 μm (A). The mean concentration of accumulated fibronectin around each spheroid is displayed as Tukey boxplots (n = 33 spheroids per condition; 2 biological repeats; Mann-Whitney test). Yellow squares indicate ROIs that are magnified (B).

(C–F) Lifeact-mRFP shCTRL or shMYO10 DCIS-like xenografts (day 25) were imaged live *ex vivo* using a spinning-disk confocal microscope (40× objective, ORCA camera). Scale bars: (main) 100 μm. Xenografts were either incubated with the fibrillar collagen probe CNA35-GFP before imaging (C and D, shCTRL xenografts) or imaged live over an extended time (E and F, shCTRL, and shMYO10 xenografts). A 3D reconstruction (C, see also Video S6) and a single z plane (D) of a representative FOV are displayed for xenografts labeled with CNA35-GFP. Representative FOVs are also shown for the extended imaging (E, see Video S6). The number of protruding cells was quantified from xenografts in (E) (n > 38 FOVs; 3 independent experiments; randomization test) and displayed as boxplots (F).

See also Figure S7 and Video S6.

model tested here, BM defects may accelerate metastasis in other contexts. Therefore, the possible anti- and pro-invasive functions of MYO10 should be carefully considered when therapeutic targeting of this protein is attempted.

Limitations of the study

Due to the limited availability of xenograft models for DCIS, the conclusions of this study are based on one model and cannot be generalized without further investigation. We uncover here a concept for filopodia regulation of the tumor-stroma border in early-stage breast cancer.

STAR★METHODS

Detailed methods are provided in the online version of this paper and include the following:

- KEY RESOURCES TABLE
- RESOURCE AVAILABILITY
  - Lead contact
  - Materials availability
  - Data and code availability
- EXPERIMENTAL MODEL AND SUBJECT DETAILS
  - Animal models
  - Human tissue samples
  - Cell lines
- METHOD DETAILS
  - Generation of tumor xenografts
  - *Ex vivo* imaging of tumor xenografts
  - Surgical procedures and intravital imaging
  - Histology and immunohistochemistry
  - RNA *in situ* hybridization
  - Quantitative RT-PCR
  - Western blotting
  - Light microscopy
  - Electron microscopy
  - Proliferation assay
  - Circular invasion assays
  - ECM remodeling assay
  - RNA sequencing and data analyses
- QUANTIFICATION AND STATISTICAL ANALYSIS

SUPPLEMENTAL INFORMATION

Supplemental information can be found online at https://doi.org/10.1016/j.devcel.2022.09.016.

ACKNOWLEDGMENTS

We thank H. Hamidi for providing feedback and editing the manuscript and the Ivaska Lab members for constructive feedback over the course of this study. The Cell Imaging and Cytometry Core facility (Turku Bioscience, University of Turku, Åbo Akademi University, and Biocenter Finland), the Finnish Functional Genomics Centre (Turku Bioscience, University of Turku, Åbo Akademi University, and Biocenter Finland), the Laboratory of Electron Microscopy and Histocore (Institute of Biomedicine, University of Turku), Central Animal Laboratory (University of Turku), and Turku Bioimaging are acknowledged for services and instrumentation and expertise. We thank Ilkka Koskivuo for providing us with clinical breast cancer tissue samples and Mitro Miihkinen, Artur Padzik, Petra Laasola, and Jenni Siivonen for assistance during the experimental work. This work was supported by the Finnish Cancer Institute (K. Albin Johansson Professorship to J.I.), Academy of Finland Research project grant (325464 to J.I.) and Center of Excellence in Biological Barrier Mechanics and Disease (346131 to J.I.), Finnish Cancer Organization (grants to J.I. and G.J.), Sigrid Jusélius Foundation (grants to J.I., E.P., and G.J.), Academy of Finland research fellowships (323096 to E.P., 338537 to G.J., and 312517 to M.G.), the Hospital District of Southwest Finland (11083 to E.P.), the University of Turku Foundation (grants to E.P. and G.J.), the Åbo Akademi University Research Foundation (CoE CellMech; to G.J.), the Solution for Health strategic funding to Åbo Akademi University (to G.J.), the Boehringer Ingelheim Foundation (Ph.D. fellowship to C.L.G.J.S.), EMBO postdoctoral fellowship (grant ALTF 1035-2020 to C.L.G.J.S.), Finnish Cultural Foundation (to A.I.), and Josef Steiner Cancer Research Foundation (to J.v.R.). This research was supported by InFLAMES Flagship Programme of the Academy of Finland (decision number: 337531 and **337530**).

AUTHOR CONTRIBUTIONS

Conceptualization, E.P., G.J., and J.I.; methodology, E.P., G.J., J.I., and C.L.G.J.S.; formal analysis, E.P., G.J., C.L.G.J.S., A.I., C.G., S.K., A.L., L.L.E., and M.G.; investigation, E.P., G.J., C.L.G.J.S., M.-C.L., L.M.K., A.I., K.T., M.G., P.B., P.H., and I.P.; writing—original draft, E.P., G.J., and J.I.; writing—review and editing, all authors; visualization, E.P., G.J., A.I., and J.I.; supervision, E.P., G.J., J.I., L.L.E., and J.v.R.; funding acquisition, E.P., G.J., and J.I.

DECLARATION OF INTERESTS

The authors declare no competing interests.

Received: March 9, 2022
Revised: August 26, 2022
Accepted: September 28, 2022
Published: October 24, 2022

REFERENCES

Albuschies, J., and Vogel, V. (2013). The role of filopodia in the recognition of nanotopographies. Sci. Rep. *3*, 1658. https://doi.org/10.1038/srep01658.

Aper, S.J.A., van Spreeuwel, A.C.C., van Turnhout, M.C., van der Linden, A.J., Pieters, P.A., van der Zon, N.L.L., de la Rambelje, S.L., Bouten, C.V.C., and Merkx, M. (2014). Colorful protein-based fluorescent probes for collagen imaging. PLoS One *9*. e114983. https://doi.org/10.1371/journal.pone.0114983.

Arganda-Carreras, I., Kaynig, V., Rueden, C., Eliceiri, K.W., Schindelin, J., Cardona, A., and Sebastian Seung, H.S. (2017). Trainable Weka segmentation: a machine learning tool for microscopy pixel classification. Bioinformatics *33*, 2424–2426. https://doi.org/10.1093/bioinformatics/btx180.

Arjonen, A., Kaukonen, R., Mattila, E., Rouhi, P., Högnäs, G., Sihto, H., Miller, B.W., Morton, J.P., Bucher, E., Taimen, P., et al. (2014a). Mutant p53-associated myosin-X upregulation promotes breast cancer invasion and metastasis. J. Clin. Invest. *124*, 1069–1082. https://doi.org/10.1172/JCI67280.

Behbod, F., Kittrell, F.S., LaMarca, H., Edwards, D., Kerbawy, S., Heestand, J.C., Young, E., Mukhopadhyay, P., Yeh, H.-W., Allred, D.C., et al. (2009). An intraductal human-in-mouse transplantation model mimics the subtypes of ductal carcinoma in situ. Breast Cancer Res *11*, R66.

Berg, J.S., and Cheney, R.E. (2002). Myosin-X is an unconventional myosin that undergoes intrafilopodial motility. Nat. Cell Biol. *4*, 246–250. https://doi.org/10.1038/ncb762.

Betsill, W.L., Rosen, P.P., Lieberman, P.H., and Robbins, G.F. (1978). Intraductal carcinoma. Long-term follow-up after treatment by biopsy alone. JAMA *239*, 1863–1867. https://doi.org/10.1001/jama.239.18.1863.

Bornschlögl, T., Romero, S., Vestergaard, C.L., Joanny, J.F., Van Nhieu, G.T.V., and Bassereau, P. (2013). Filopodial retraction force is generated by cortical actin dynamics and controlled by reversible tethering at the tip. Proc. Natl. Acad. Sci. USA *110*, 18928–18933. https://doi.org/10.1073/pnas.1316572110.

Brockman, J.M., Su, H., Blanchard, A.T., Duan, Y., Meyer, T., Quach, M.E., Glazier, R., Bazrafshan, A., Bender, R.L., Kellner, A.V., et al. (2020). Live-cell super-resolved PAINT imaging of piconewton cellular traction forces. Nat. Methods *17*, 1018–1024. https://doi.org/10.1038/s41592-020-0929-2.

Cao, R., Chen, J., Zhang, X., Zhai, Y., Qing, X., Xing, W., Zhang, L., Malik, Y.S., Yu, H., and Zhu, X. (2014). Elevated expression of myosin X in tumours contributes to breast cancer aggressiveness and metastasis. Br. J. Cancer *111*, 539–550. https://doi.org/10.1038/bjc.2014.298.

Clark, A.G., and Vignjevic, D.M. (2015). Modes of cancer cell invasion and the role of the microenvironment. Curr. Opin. Cell Biol. *36*, 13–22. https://doi.org/10.1016/j.ceb.2015.06.004.

Cojoc, D., Difato, F., Ferrari, E., Shahapure, R.B., Laishram, J., Righi, M., Di Fabrizio, E.M.D., and Torre, V. (2007). Properties of the force exerted by filopodia and lamellipodia and the involvement of cytoskeletal components. PLoS One *2*, e1072. https://doi.org/10.1371/journal.pone.0001072.

Dawson, P.J., Wolman, S.R., Tait, L., Heppner, G.H., and Miller, F.R. (1996). MCF10AT: a model for the evolution of cancer from proliferative breast disease. Am. J. Pathol. *148*, 313–319.

Dobin, A., Davis, C.A., Schlesinger, F., Drenkow, J., Zaleski, C., Jha, S., Batut, P., Chaisson, M., and Gingeras, T.R. (2013). STAR: ultrafast universal RNA-seq aligner. Bioinformatics *29*, 15–21. https://doi.org/10.1093/bioinformatics/bts635.

Eddy, R.J., Weidmann, M.D., Sharma, V.P., and Condeelis, J.S. (2017). Tumor cell invadopodia: invasive protrusions that orchestrate metastasis. Trends Cell Biol. *27*, 595–607. https://doi.org/10.1016/j.tcb.2017.03.003.

Ershov, D., Phan, M.S., Pylvänäinen, J.W., Rigaud, S.U., Le Blanc, L., Charles-Orszag, A., Conway, J.R.W., Laine, R.F., Roy, N.H., Bonazzi, D., et al. (2022). TrackMate 7: integrating state-of-the-art segmentation algorithms into tracking pipelines. Nat. Methods *19*, 829–832. https://doi.org/10.1038/s41592-022-01507-1.

Fazeli, E., Roy, N.H., Follain, G., Laine, R.F., von Chamier, L., Hänninen, P.E., Eriksson, J.E., Tinevez, J.Y., and Jacquemet, G. (2020). Automated cell tracking using StarDist and TrackMate. F1000Res *9*, 1279. https://doi.org/10.12688/f1000research.27019.1.

Ferlay, J., Colombet, M., Soerjomataram, I., Dyba, T., Randi, G., Bettio, M., Gavin, A., Visser, O., and Bray, F. (2018). Cancer incidence and mortality patterns in Europe: estimates for 40 countries and 25 major cancers in 2018. Eur. J. Cancer *103*, 356–387. https://doi.org/10.1016/j.ejca.2018.07.005.

Ferrari, R., Martin, G., Tagit, O., Guichard, A., Cambi, A., Voituriez, R., Vassilopoulos, S., and Chavrier, P. (2019). MT1-MMP directs force-producing proteolytic contacts that drive tumor cell invasion. Nat. Commun. *10*, 4886. https://doi.org/10.1038/s41467-019-12930-y.

Fierro-González, J.C., White, M.D., Silva, J.C., and Plachta, N. (2013). Cadherin-dependent filopodia control preimplantation embryo compaction. Nat. Cell Biol. *15*, 1424–1433. https://doi.org/10.1038/ncb2875.

Gentleman, R.C., Carey, V.J., Bates, D.M., Bolstad, B., Dettling, M., Dudoit, S., Ellis, B., Gautier, L., Ge, Y., Gentry, J., et al. (2004). Bioconductor: open software development for computational biology and bioinformatics. Genome Biol. *5*, R80. https://doi.org/10.1186/gb-2004-5-10-r80.

Glentis, A., Oertle, P., Mariani, P., Chikina, A., El Marjou, F., Attieh, Y., Zaccarini, F., Lae, M., Loew, D., Dingli, F., et al. (2017). Cancer-associated fibroblasts induce metalloprotease-independent cancer cell invasion of the basement membrane. Nat. Commun. *8*, 924. https://doi.org/10.1038/s41467-017-00985-8.

Goedhart, J. (2019). PlotsOfDifferences – a web app for the quantitative comparison of unpaired data. Preprint at bioRxiv. https://doi.org/10.1101/578575.

Goedhart, J. (2021). SuperPlotsOfData—a web app for the transparent display and quantitative comparison of continuous data from different conditions. Mol. Biol. Cell *32*, 470–474. https://doi.org/10.1091/mbc.E20-09-0583.

Goedhart, J., and Luijsterburg, M.S. (2020). VolcaNoseR is a web app for creating, exploring, labeling and sharing volcano plots. Sci. Rep. *10*, 20560. https://doi.org/10.1038/s41598-020-76603-3.

Goncharova, A.S., Honigmann, A., Jug, F., and Krull, A. (2020). Improving blind spot denoising for microscopy. Lecture Notes in Computer Science. European Conference on Computer Vision, ECCV 2020: Computer Vision – ECCV 2020 Workshops, 380–393.

Huang, da W., Sherman, B.T., and Lempicki, R.A. (2009). Systematic and integrative analysis of large gene lists using DAVID bioinformatics resources. Nat. Protoc. *4*, 44–57. https://doi.org/10.1038/nprot.2008.211.

Jacquemet, G. (2020). Combining StarDist and TrackMate example 1 – breast cancer cell dataset. https://doi.org/10.5281/zenodo.4034976.

Jacquemet, G., Baghirov, H., Georgiadou, M., Sihto, H., Peuhu, E., Cettour-Janet, P., He, T., Perälä, M., Kronqvist, P., Joensuu, H., and Ivaska, J. (2016). L-type calcium channels regulate filopodia stability and cancer cell invasion downstream of integrin signalling. Nat. Commun. *7*, 13297. https://doi.org/10.1038/ncomms13297.

Jacquemet, G., Hamidi, H., and Ivaska, J. (2015). Filopodia in cell adhesion, 3D migration and cancer cell invasion. Curr. Opin. Cell Biol. *36*, 23–31.

Jacquemet, G., Paatero, I., Carisey, A.F., Padzik, A., Orange, J.S., Hamidi, H., and Ivaska, J. (2017). FiloQuant reveals increased filopodia density during breast cancer progression. J. Cell Biol. *216*, 3387–3403. https://doi.org/10.1083/jcb.201704045.

Jacquemet, G., Stubb, A., Saup, R., Miihkinen, M., Kremneva, E., Hamidi, H., and Ivaska, J. (2019). Filopodome mapping identifies p130Cas as a mechanosensitive regulator of filopodia stability. Curr. Biol. *29*. 202–216.e7. https://doi.org/10.1016/j.cub.2018.11.053.

Jayadev, R., and Sherwood, D.R. (2017). Basement membranes. Curr. Biol. *27*, R207–R211. https://doi.org/10.1016/j.cub.2017.02.006.

Keeley, D.P., Hastie, E., Jayadev, R., Kelley, L.C., Chi, Q., Payne, S.G., Jeger, J.L., Hoffman, B.D., and Sherwood, D.R. (2020). Comprehensive endogenous tagging of basement membrane components reveals dynamic movement within the matrix scaffolding. Dev. Cell *54*. 60–74.e7. https://doi.org/10.1016/j.devcel.2020.05.022.

Kenchappa, R.S., Mistriotis, P., Wisniewski, E., Bhattacharya, S., Kulkarni, T., West, R., Luu, A., Conlon, M., Heimsath, E., Crish, J.F., et al. (2020). Myosin 10 regulates invasion, mitosis, and metabolic signaling in glioblastoma. iScience *23*, 101802. https://doi.org/10.1016/j.isci.2020.101802.

Kluin, R.J.C., Kemper, K., Kuilman, T., de Ruiter, J.R., Iyer, V., Forment, J.V., Cornelissen-Steijger, P., de Rink, I., ter Brugge, P., Song, J.Y., et al. (2018). XenofilteR: computational deconvolution of mouse and human reads in tumor xenograft sequence data. BMC Bioinformatics *19*, 366. https://doi.org/10.1186/s12859-018-2353-5.

Kozma, K.J., Done, S.J., and Egan, S.E. (2021). The tumor cell-derived matrix of lobular breast cancer: a new vulnerability. EMBO Mol. Med. *13*, e13807. https://doi.org/10.15252/emmm.202013807.

Laine, R.F., Arganda-Carreras, I., Henriques, R., and Jacquemet, G. (2021). Avoiding a replication crisis in deep-learning-based BioImage analysis. Nat. Methods *18*, 1136–1144. https://doi.org/10.1038/s41592-021-01284-3.

Leijnse, N., Oddershede, L.B., and Bendix, P.M. (2015). Helical buckling of actin inside filopodia generates traction. Proc. Natl. Acad. Sci. USA *112*, 136–141. https://doi.org/10.1073/pnas.1411761112.

Liao, Y., Smyth, G.K., and Shi, W. (2014). featureCounts: an efficient general purpose program for assigning sequence reads to genomic features. Bioinformatics *30*, 923–930. https://doi.org/10.1093/bioinformatics/btt656.

Lodillinsky, C., Infante, E., Guichard, A., Chaligné, R., Fuhrmann, L., Cyrta, J., Irondelle, M., Lagoutte, E., Vacher, S., Bonsang-Kitzis, H., et al. (2016). p63/MT1-MMP axis is required for in situ to invasive transition in basal-like breast cancer. Oncogene *35*, 344–357. https://doi.org/10.1038/onc.2015.87.

Lord, S.J., Velle, K.B., Mullins, R.D., and Fritz-Laylin, L.K. (2020). SuperPlots: communicating reproducibility and variability in cell biology. J. Cell Biol. *219*. e202001064. https://doi.org/10.1083/jcb.202001064.

Lu, J., Doyle, A.D., Shinsato, Y., Wang, S., Bodendorfer, M.A., Zheng, M., and Yamada, K.M. (2020). Basement membrane regulates fibronectin organization using sliding focal adhesions driven by a contractile winch. Dev. Cell *52*. 631–646.e4. https://doi.org/10.1016/j.devcel.2020.01.007.

Lukinavičius, G., Blaukopf, C., Pershagen, E., Schena, A., Reymond, L., Derivery, E., Gonzalez-Gaitan, M., D'Este, E., Hell, S.W., Wolfram Gerlich, D.W., and Johnsson, K. (2015). SiR–Hoechst is a far-red DNA stain for live-cell nanoscopy. Nat. Commun. *6*, 8497. https://doi.org/10.1038/ncomms9497.

Malandrino, A., Trepat, X., Kamm, R.D., and Mak, M. (2019). Dynamic filopodial forces induce accumulation, damage, and plastic remodeling of 3D extracellular matrices. PLoS Comput. Biol. *15*. e1006684. https://doi.org/10.1371/journal.pcbi.1006684.

Matsubayashi, Y., Sánchez-Sánchez, B.J., Marcotti, S., Serna-Morales, E., Dragu, A., Díaz-de-la-Loza, M.D., Vizcay-Barrena, G., Fleck, R.A., and Stramer, B.M. (2020). Rapid homeostatic turnover of embryonic ECM during tissue morphogenesis. Dev. Cell *54*. 33–42.e9. https://doi.org/10.1016/j.devcel.2020.06.005.

McCarthy, D.J., Chen, Y., and Smyth, G.K. (2012). Differential expression analysis of multifactor RNA-Seq experiments with respect to biological variation. Nucleic Acids Res. *40*, 4288–4297. https://doi.org/10.1093/nar/gks042.

Messal, H.A., van Rheenen, J., and Scheele, C.L.G.J. (2021). An intravital microscopy toolbox to study mammary gland dynamics from cellular level to organ scale. J. Mammary Gland Biol. Neoplasia *26*, 9–27. https://doi.org/10.1007/s10911-021-09487-2.

Miihkinen, M., Grönloh, M.L.B., Popović, A., Vihinen, H., Jokitalo, E., Goult, B.T., Ivaska, J., and Jacquemet, G. (2021). Myosin-X and talin modulate integrin activity at filopodia tips. Cell Rep. *36*, 109716. https://doi.org/10.1016/j.celrep.2021.109716.

Miller, F.R., Santner, S.J., Tait, L., and Dawson, P.J. (2000). MCF10DCIS.com xenograft model of human comedo ductal carcinoma in situ. J. Natl. Cancer Inst. *92*, 1185–1186.

Monteiro, P., Rossé, C., Castro-Castro, A., Irondelle, M., Lagoutte, E., Paul-Gilloteaux, P., Desnos, C., Formstecher, E., Darchen, F., Perrais, D., et al. (2013). Endosomal WASH and exocyst complexes control exocytosis of MT1-MMP at invadopodia. J. Cell Biol. *203*, 1063–1079. https://doi.org/10.1083/jcb.201306162.

Naba, A., Clauser, K.R., Ding, H., Whittaker, C.A., Carr, S.A., and Hynes, R.O. (2016). The extracellular matrix: tools and insights for the "omics" era. Matrix Biol. *49*, 10–24. https://doi.org/10.1016/j.matbio.2015.06.003.

Naba, A., Clauser, K.R., Hoersch, S., Liu, H., Carr, S.A., and Hynes, R.O. (2012). The matrisome: in silico definition and in vivo characterization by proteomics of normal and tumor extracellular matrices. Mol. Cell. Proteomics *11*. M111.014647. https://doi.org/10.1074/mcp.M111.014647.

Naba, A., Clauser, K.R., Lamar, J.M., Carr, S.A., and Hynes, R.O. (2014). Extracellular matrix signatures of human mammary carcinoma identify novel metastasis promoters. eLife *3*, e01308. https://doi.org/10.7554/eLife.01308.

Naba, A., Pearce, O.M.T., Del Rosario, A., Ma, D., Ding, H., Rajeeve, V., Cutillas, P.R., Balkwill, F.R., and Hynes, R.O. (2017). Characterization of the extracellular matrix of normal and diseased tissues using proteomics. J. Proteome Res. *16*, 3083–3091. https://doi.org/10.1021/acs.jproteome.7b00191.

Piersma, B., Hayward, M.K., and Weaver, V.M. (2020). Fibrosis and cancer: a strained relationship. Biochim. Biophys. Acta Rev. Cancer *1873*, 188356. https://doi.org/10.1016/j.bbcan.2020.188356.

Postma, M., and Goedhart, J. (2019). PlotsOfData—a web app for visualizing data together with their summaries. PLoS Biol. *17*. e3000202. https://doi.org/10.1371/journal.pbio.3000202.

Risom, T., Glass, D.R., Averbukh, I., Liu, C.C., Baranski, A., Kagel, A., McCaffrey, E.F., Greenwald, N.F., Rivero-Gutiérrez, B., Strand, S.H., et al. (2022). Transition to invasive breast cancer is associated with progressive changes in the structure and composition of tumor stroma. Cell *185*. 299–310.e18. https://doi.org/10.1016/j.cell.2021.12.023.

Ritchie, M.E., Phipson, B., Wu, D., Hu, Y., Law, C.W., Shi, W., and Smyth, G.K. (2015). limma powers differential expression analyses for RNA-sequencing and microarray studies. Nucleic Acids Res. *43*, e47. https://doi.org/10.1093/nar/gkv007.

Ryser, M.D., Weaver, D.L., Zhao, F., Worni, M., Grimm, L.J., Gulati, R., Etzioni, R., Hyslop, T., Lee, S.J., and Hwang, E.S. (2019). Cancer outcomes in DCIS patients without locoregional treatment. J. Natl. Cancer Inst. *111*, 952–960. https://doi.org/10.1093/jnci/djy220.

Sato, Y., Nagatoshi, K., Hamano, A., Imamura, Y., Huss, D., Uchida, S., and Lansford, R. (2017). Basal filopodia and vascular mechanical stress organize fibronectin into pillars bridging the mesoderm-endoderm gap. Development *144*, 281–291. https://doi.org/10.1242/dev.141259.

Schedin, P., and Keely, P.J. (2011). Mammary gland ECM remodeling, stiffness, and mechanosignaling in normal development and tumor progression. Cold Spring Harb. Perspect. Biol. *3*, a003228. https://doi.org/10.1101/cshperspect.a003228.

Schindelin, J., Arganda-Carreras, I., Frise, E., Kaynig, V., Longair, M., Pietzsch, T., Preibisch, S., Rueden, C., Saalfeld, S., Schmid, B., et al. (2012). Fiji: an open-source platform for biological-image analysis. Nat. Methods *9*, 676–682. https://doi.org/10.1038/nmeth.2019.

Schmidt, U., Weigert, M., Broaddus, C., and Myers, G. (2018). Cell detection with star-convex polygons. In Medical Image Computing and Computer Assisted Intervention – MICCAI 2018, A.F. Frangi, J.A. Schnabel, C. Davatzikos, C. Alberola-López, and G. Fichtinger, eds. (Springer International Publishing), pp. 265–273.

Sflomos, G., Battista, L., Aouad, P., De Martino, F., Scabia, V., Stravodimou, A., Ayyanan, A., Ifticene-Treboux, A.; RLS, and Bucher, P., et al. (2021). Intraductal xenografts show lobular carcinoma cells rely on their own extracellular matrix and LOXL1. EMBO Mol. Med. *13*, e13180. https://doi.org/10.15252/emmm.202013180.

Shibue, T., Brooks, M.W., Inan, M.F., Reinhardt, F., and Weinberg, R.A. (2012). The outgrowth of micrometastases is enabled by the formation of filopodium-like protrusions. Cancer Discov. *2*, 706–721. https://doi.org/10.1158/2159-8290.CD-11-0239.

Shibue, T., Brooks, M.W., and Weinberg, R.A. (2013). An integrin-linked machinery of cytoskeletal regulation that enables experimental tumor initiation and metastatic colonization. Cancer Cell *24*, 481–498. https://doi.org/10.1016/j.ccr.2013.08.012.

Singh, P., Carraher, C., and Schwarzbauer, J.E. (2010). Assembly of fibronectin extracellular matrix. Annu. Rev. Cell Dev. Biol. *26*, 397–419. https://doi.org/10.1146/annurev-cellbio-100109-104020.

Stubb, A., Laine, R.F., Miihkinen, M., Hamidi, H., Guzmán, C., Henriques, R., Jacquemet, G., and Ivaska, J. (2020). Fluctuation-based super-resolution traction force microscopy. Nano Lett. *20*, 2230–2245. https://doi.org/10.1021/acs.nanolett.9b04083.

Summerbell, E.R., Mouw, J.K., Bell, J.S.K., Knippler, C.M., Pedro, B., Arnst, J.L., Khatib, T.O., Commander, R., Barwick, B.G., Konen, J., et al. (2020). Epigenetically heterogeneous tumor cells direct collective invasion through filopodia-driven fibronectin micropatterning. Sci. Adv. *6*, eaaz6197. https://doi.org/10.1126/sciadv.aaz6197.

Tinevez, J.Y., Perry, N., Schindelin, J., Hoopes, G.M., Reynolds, G.D., Laplantine, E., Bednarek, S.Y., Shorte, S.L., and Eliceiri, K.W. (2017). TrackMate: an open and extensible platform for single-particle tracking. Methods *115*, 80–90. https://doi.org/10.1016/j.ymeth.2016.09.016.

Tokuo, H., Bhawan, J., and Coluccio, L.M. (2018). Myosin X is required for efficient melanoblast migration and melanoma initiation and metastasis. Sci. Rep. *8*, 10449. https://doi.org/10.1038/s41598-018-28717-y.

Valenzuela, J.I., and Perez, F. (2020). Localized intercellular transfer of ephrin-as by trans-endocytosis enables long-term signaling. Dev. Cell *52*. 104–117. e5. https://doi.org/10.1016/j.devcel.2019.11.013.

von Chamier, L., Laine, R.F., Jukkala, J., Spahn, C., Krentzel, D., Nehme, E., Lerche, M., Hernández-Pérez, S., Mattila, P.K., Karinou, E., et al. (2021). Democratising deep learning for microscopy with ZeroCostDL4Mic. Nat. Commun. *12*, 2276. https://doi.org/10.1038/s41467-021-22518-0.

Waclaw, B., Bozic, I., Pittman, M.E., Hruban, R.H., Vogelstein, B., and Nowak, M.A. (2015). A spatial model predicts that dispersal and cell turnover limit intratumour heterogeneity. Nature *525*, 261–264. https://doi.org/10.1038/nature14971.

Wang, H., Lacoche, S., Huang, L., Xue, B., and Muthuswamy, S.K. (2013). Rotational motion during three-dimensional morphogenesis of mammary epithelial acini relates to laminin matrix assembly. Proc Natl Acad Sci U S A *110*, 163–168.

Wortel, I.M.N., Dannenberg, K., Berry, J.C., Miller, M.J., and Textor, J. (2019). CelltrackR: an R package for fast and flexible analysis of immune cell migration data. ImmunoInformatics *1–2*, 100003.

Yurchenco, P.D., and Patton, B.L. (2009). Developmental and pathogenic mechanisms of basement membrane assembly. Curr. Pharm. Des. *15*, 1277–1294. https://doi.org/10.2174/138161209787846766.

STAR★METHODS

KEY RESOURCES TABLE

REAGENT or RESOURCE	SOURCE	IDENTIFIER
Antibodies		
Rabbit polyclonal anti-collagen IV antibody (IHC, 1:400; WB, 1:1000)	Abcam	Cat#ab19808; RRID: AB_445160
Mouse monoclonal anti-β-actin (clone AC-15) (WB, 1:1000)	Sigma-Aldrich	Cat#ab1218; RRID: AB_298911
Mouse monoclonal anti-GAPDH (clone 6C5cc) (WB, 1:1000)	HyTest	Cat#5G4 / 5G4cc; RRID: AB_2858176
Rabbit polyclonal anti-fibronectin antibody (IHC, 1:400; WB, 1:1000)	Merck	Cat#F3648; RRID: AB_476976
Rabbit polyclonal anti-MYO10 antibody (WB, 1:1000)	Novus Biologicals	Cat#22430002; RRID: AB_2148055
Rabbit polyclonal anti-GFP antibody (WB, 1:1000)	Abcam	Cat#Ab290; RRID: AB_303395
Mouse monoclonal anti-alpha-smooth muscle actin (αSMA, clone 1A4) antibody (IHC, 1:1000)	Merck	Cat#A2547; RRID: AB_476701
Rabbit monoclonal anti-slug (clone C19G7) antibody (IHC, 1:100)	Cell Sig. Techchnology	Cat#9585; RRID: AB_2239535
Mouse monoclonal anti-vimentin (Clone V9) antibody (IHC, 1:200)	Santa Cruz	Cat#sc-6260; RRID: AB_628437
Mouse Monoclonal anti-mitochondria ((clone 113-1) antibody (IHC, 1:100)	Millipore	Cat#MAB1273; RRID: AB_94052
Mouse monoclonal anti-p63 (clone 4A4) antibody (IHC, 1:100)	Abcam	Cat#ab3239; RRID: AB_303633
Rabbit polyclonal anti-laminin antibody (IHC, 1:100)	Novus Biologicals	Cat# NB300-144; RRID: AB_350469
Rabbit polyclonal anti-MYO10 antibody (IHC, 1:100)	Merck	HPA024223; RRID: AB_1854248
Rat monoclonal anti-active integrin beta-1 (clone 9EG7) antibody	BD Pharmingen	Cat#553715; RRID: AB_395001
Mouse monoclonal anti-inactive integrin beta-1 (clone AIIB2)	in-house hybridoma production	N/A
Rat monoclonal anti-keratin 8 (KRT8) antibody (IHC; FFPE 1:2000, Frozen sections 1:1000)	DSHB	Cat#TROMA-I; RRID: AB_531826
Donkey anti-Rabbit IgG (H+L) Highly Cross-Adsorbed Secondary Antibody, Alexa Fluor™ 488	Thermo Fisher Scientific	Cat#A-21206; RRID: AB_2535792
Goat anti-Rat IgG (H+L) Cross-Adsorbed Secondary Antibody, Alexa Fluor™ 568	Thermo Fisher Scientific	Cat#A-11077; RRID: AB_2534121
Donkey anti-Mouse IgG (H+L) Highly Cross-Adsorbed Secondary Antibody, Alexa Fluor™ 647	Thermo Fisher Scientific	Cat#A-31571; RRID: AB_162542
Bacterial and virus strains		
MISSION® pLKO.1-puro Non-Target shRNA Control	Merck	Cat#SHC016V-1EA
shRNA targeting human MYO10 (shMYO10 #3)	Merck	TRC clone ID:TRCN0000123087
shRNA targeting human MYO10 (shMYO10 #4)	Merck	TRC clone ID:TRCN0000123088
Chemicals, peptides, and recombinant proteins		
Horse serum	Thermo Fisher Scientific	Cat#16050122
Human EGF	Merck	Cat#E9644
Hydrocortisone	Merck	Cat#H0888-1G

(*Continued on next page*)

Continued

REAGENT or RESOURCE	SOURCE	IDENTIFIER
Cholera toxin	Merck	Cat#C8052-1MG
Insulin	Merck	Cat#I9278-5ML
Penicillin/streptomycin	Merck	Cat#P0781- 100ML
Bovine plasma fibronectin	Merck	Cat#341631
RFP-Booster Atto594	Chromotek	Cat#rb2AF568
SiR-DNA (SiR-Hoechst)	Tebu-bio (Lukinavičius et al., 2015)	Cat#SC007
Growth factor reduced Matrigel	BD Biosciences	Cat#354230
PureCol EZ Gel (fibrillar collagen I, concentration 5 mg/ml)	Advanced BioMatrix	Cat#5074
FITC-collagen (type I, bovine skin)	Merck	Cat#C4361
Fluorescently labeled fibronectin (HiLyte Fluor 488-labeled fibronectin)	Cytoskeleton	Cat#FNR02
Fluorescently labeled laminin-111 (HiLyte Fluor 488-labeled laminin-111)	Cytoskeleton	Cat#LMN02
Myosin II inhibitor (-)-blebbistatin	Stemcell Technologies	Cat#72402
Saracatinib	Selleck chemicals	Cat#S1006
Critical commercial assays		
RNAscope™ 2.5 HD Detection kit (BROWN)	Advanced Cell Diagnostics	Cat#322300
Deposited data		
Raw and analyzed data	This paper	GEO: GSE166898
Experimental models: Cell lines		
MCF10 DCIS.COM	J.F. Marshall (Barts Cancer Institute, Queen Mary University of London, London, UK) (Miller et al., 2000)	RRID:CVCL_5552
lifeact-mRFP DCIS.COM	(Jacquemet et al., 2017)	N/A
lifeact-mRFP shMYO10 DCIS.COM	This paper	N/A
lifeact-mRFP shCTRL DCIS.COM	This paper	N/A
lifeact-mRFP GFP shMYO10 DCIS.COM	This paper	N/A
lifeact-mRFP GFP shCTRL DCIS.COM	This paper	N/A
Experimental models: Organisms/strains		
6-7 -week-old virgin female NOD.scid mice	Envigo	Order code: 170
6-7 -week-old virgin female NOD.scid mice	The Jackson Laboratory	005557
Oligonucleotides		
RNAscope™ MYO10 mRNA Probe – Hs-MYO10-full	Advanced Cell Diagnostics	Cat#440691
RNAscope™ Negative Control Probe – DapB (bacterial gene)	Advanced Cell Diagnostics	Cat#310043
RNAscope™ Positive Control Probe – Hs-PPIB (human peptidylprolyl isomerase B)	Advanced Cell Diagnostics	Cat#313901
Software and algorithms		
Fiji	Schindelin et al., 2012	https://fiji.sc/
FiloQuant	Jacquemet et al., 2017	https://imagej.net/plugins/filoquant
ZeroCostDL4Mic platform	von Chamier et al., 2021	https://github.com/HenriquesLab/ZeroCostDL4Mic/wiki
TrackMate	Tinevez et al., 2017; Ershov et al., 2022	https://imagej.net/plugins/trackmate/
StarDist	Schmidt et al., 2018	https://imagej.net/plugins/stardist
Other		
StarDist Model and training dataset (breast cancer cell dataset)	Zenodo; Jacquemet, 2020	https://doi.org/10.5281/zenodo.4034976

RESOURCE AVAILABILITY

Lead contact

Further information and requests for resources and reagents should be directed to and will be fulfilled by the lead contact, Johanna Ivaska (johanna.ivaska@utu.fi).

Materials availability

The DCIS.com lifeact-RFP shCTRL and shMYO10 cell lines are available from the lead contact upon request.

Data and code availability

The RNA sequencing data have been deposited at Gene Expression Omnibus (GEO) and are publicly available as of the date of publication (GEO accession number: GSE166898). The accession number is listed in the key resources table. The StarDist model used to automatically track cells is available on Zenodo (Jacquemet, 2020).

This paper does not report original code.

Any additional information required to reanalyze the data reported in this paper will be shared by the lead contact upon request.

EXPERIMENTAL MODEL AND SUBJECT DETAILS

Animal models

Six-seven-week-old virgin female NOD.CB17-Prkdc^{scid}/NCrHsd (Envigo) or NOD-Scid IL2Rgnull (The Jackson Laboratory, strain 005557; for intravital imaging) were used in tumor xenograft models. Mice were housed in standard conditions (12 h light/dark cycle) with food (irradiated normal chow) and water available *ad libitum*, and randomly assigned to experimental groups. The National Animal Experiment Board authorized all animal studies, and per The Finnish Act on Animal Experimentation (Animal license number ESAVI-9339-04.10.07-2016; Netherlands Cancer Institute NVWA license number 30100, Project number AVD301002015125).

Human tissue samples

Human breast tissue samples were obtained at the Department of Plastic and General Surgery at Turku University Hospital (Turku, Finland) with approval from the Ethics Committee of the Hospital District of Southwestern Finland (permit number 23/1801/2018), and written consent from the patients (§279, 9/2001). Normal breast samples were obtained from three female patients undergoing a reduction mammoplasty operation (age 18-26). Paired samples from breast tumors and the surrounding peritumoral or contralateral normal breast tissues of six female breast cancer patients (age 41-85) were excised and examined by a clinical pathologist. Tissue samples were processed to frozen tissue sections or formalin-fixed paraffin-embedded (FFPE) tissue sections.

Cell lines

MCF10 DCIS.com cells (DCIS.com; invasive T24 c-Ha-ras oncogene-transfected breast epithelial cells) were provided by J.F. Marshall (Barts Cancer Institute, Queen Mary University of London, London, England, UK). The generation of DCIS.com cells is described in (Miller et al., 2000). DCIS.com lifeact-RFP cells were generated previously (Jacquemet et al., 2017) through lentiviral transduction using pCDH-lifeAct mRFP, psPAX2, and pMD2.G constructs and cultured in a 1:1 mix of DMEM (Merck) and F12 (Merck) supplemented with 5% horse serum (GIBCO BRL, Cat Number: 16050122), 20 ng/ml human EGF (Merck, Cat Number: E9644), 0.5 mg/ml hydrocortisone (Merck, Cat Number: H0888-1G), 100 ng/ml cholera toxin (Merck, Cat Number: C8052-1MG), 10 μg/ml insulin (Merck, Cat Number: I9278-5ML), and 1% (vol/vol) penicillin/streptomycin (Merck, Cat Number: P0781- 100ML) at 37°C, 5% CO_2.

The DCIS.com lifeact-RFP shCTRL #s, shMYO10 #3 and shMYO10 #4 cell lines were generated using lentiviral particles containing a non-target control shRNA (Merck, Cat Number: SHC016V-1EA) or shRNA targeting human MYO10 (shMYO10 #3, TRCN0000123087; shMYO10 #4, TRCN0000123088), respectively. Transduced cells were selected using normal media supplemented with 2 $\mu g.ml^{-1}$ of puromycin. DCIS.com lifeact-RFP shCTRL and shMYO10 lines were generated from single-cell clones obtained from the DCIS.com lifeact-RFP shMYO10 #3 and shMYO10 #4 cell lines. Four single-cell clones with normal MYO10 levels were pooled to create the shCTRL line, and four single-cell clones with very low MYO10 levels were pooled to create the shMYO10 line. The DCIS.com lifeact-RFP shCTRL and shMYO10 GFP lines were generated using lentiviral particles containing GFP. Positive cells were sorted using a BD FACSaria II cell sorter (Becton Dickinson) with a gating strategy to obtain medium expression.

Cell lines were not authenticated but were routinely monitored for mycoplasma contamination.

METHOD DETAILS

Generation of tumor xenografts

For xenografts, 1×10^5 DCIS.com lifeact-RFP cells were resuspended in 100 μl of a mixture of 50% Matrigel (diluted in PBS) before being injected subcutaneously in the flank or orthotopically in the abdominal mammary gland of 6-7-week-old virgin female NOD.scid mice (Envigo). Tumor growth was measured with a caliper 1-2 times per week. Mice were sacrificed 10-25 days post-inoculation (as indicated), and the tumors were dissected.

Ex vivo imaging of tumor xenografts

To perform ex-vivo imaging, DCIS-like xenografts were dissected 25 days post-inoculation, incubated with the fibrillar collagen probe CNA35-GFP (when indicated, produced in-house (Aper et al., 2014)), deposited in a glass-bottom dish (coverslip No. 0; MatTek), and embedded in a collagen-I gel (Advanced BioMatrix, Cat Number: 5074). The gel was then allowed to polymerize at 37°C for 15 min, and the DCIS.com culture medium was added on top. Xenografts were then imaged live using a spinning-disk confocal microscope (40x objective, imaging starting less than 1 h post dissection). Images were processed using Fiji. 3D visualizations were performed using Imaris (Oxford Instruments) and Arivis Vision4D (Arivis).

Surgical procedures and intravital imaging

Tumor-bearing mice were anesthetized with a 1.5%-2% isoflurane/air mixture 25-35 days post tumor inoculation. To visualize the subcutaneous tumors, a skin flap surgery was performed. The area around the tumor was shaved, disinfected, and a vertical midline incision was made through the skin, followed by two horizontal incisions anterior and posterior of the tumor area. The skin was detached from the underlying tissues and peritoneum by blunt dissection/gentle pulling with a curved instrument. The mouse was transferred to a custom-made imaging box connected to an isoflurane vaporizer. The mouse was placed on top of a metal inlay with a rectangular opening covered with a coverglass. The skin flap was opened, and the tumor area was placed on the coverglass. A sterile gauze soaked in preheated PBS was placed on top of the skin flap to maintain hydration, and parafilm was used to cover the skin flap and create a humidified chamber. To visualize the orthotopic tumors, implantation of an optical imaging window was carried out as described by (Messal et al., 2021). In short, the tumor area was shaved and disinfected, and a 10-15 mm incision was made above the tumor. The skin was loosened from the tumor tissue by blunt dissection, and a non-absorbable silk suture was placed in loops around the incision. A sterilized titanium mammary imaging window with a fixed glass coverslip was inserted and secured in the skin with the purse-string suture. After window implantation, the mouse was transferred to a custom-designed imaging box on top of an inlay designed with a hole to secure the imaging window. During time-lapse imaging, the mouse received nutrition through a subcutaneously placed flexible needle (100 μl/hr, Nutriflex (R) special 70/240). Intravital imaging was conducted with an inverted Leica SP8 DIVE microscope (Leica Microsystems) equipped with four tunable hybrid detectors, a MaiTai eHP DeepSee laser (Spectra-Physics), and an InSight X3 laser (Spectra-Physics). For image acquisition, Leica Application Suite X (LAS X) was used.

All images were collected at 12 bit and acquired with a 25x water immersion objective with a free working distance of 2.40 mm (HC FLUOTAR L 25x/0.95 W VISIR 0.17). GFP and mRFP were excited with 925 nm and 960 nm and detected between 490-550 nm and 580-650 nm, respectively. The second-harmonic generation signal was collected to visualize Collagen I. Whole-tumor areas were imaged by 3D tiles scan imaging with a z-step size of 6 μm. Timelapse imaging of regions of interest (XYZT) was performed at 5- or 20-min time intervals for up to 12 h. Imaged regions were stitched over time using Leica LASX software, and XYZ-drift corrections were performed using Huygens Object Stabilizer software (Scientific Volume Imaging). 3D renderings displayed in Video S3 were created using the LAS X 3D Visualization module. Motile cells were manually tracked using Imaris software (version 9.0, Oxford Instruments). The mean track speed and persistence were quantified along with the number of invasive (protruding/motile) GFP-positive cells per FOV. Image sequences with high cell blebbing (apoptosis due to limited blood supply) were excluded.

Histology and immunohistochemistry

FFPE mouse xenograft tissues were sectioned and H&E-labelled with standard procedures. Xenograft histology was scored blindly (*in situ* tumor / *in situ* tumor with disorganized areas or partial invasion / tumor with invasion). Immunohistochemistry of FFPE sections was performed with standard protocols on deparaffinized sections after heat-mediated antigen retrieval in Universal buffer (Retriever 2100, Aptum Bio) with the indicated antibodies. All samples were stained with DAPI (4′,6-diamidino-2-phenylindole, dihydrochloride; Life Technologies), mounted in Mowiol containing DABCO® (Merck) antifade reagent, and imaged with spinning-disk microscopy.

The percentage of GFP-positive cells at the edges of tumor acini was analyzed using Fiji (Schindelin et al., 2012). For each set of samples, four images were acquired: cancer cell marker (human mitochondria), ECM marker (Collagen IV), nuclei (DAPI), and GFP. The edge of tumor acini and its coordinates were first defined using the cancer cell and ECM markers. Then each cell was identified using the DAPI label, and its distance to the closest edge of tumor acini was calculated with R software. Using this information, cells were classified as edge cells (< than 10 μm distance) or not edge cells (> than 10 μm distance). Finally, the GFP channel was used to separate the GFP-positive cells from GFP-negative and quantify the percentage of GFP-positive cells at the edge of tumor acini.

For immunohistochemistry of frozen tissue sections, healthy human breast and breast cancer samples were fixed overnight at +4°C in periodate–lysine–paraformaldehyde (PLP) buffer [1% paraformaldehyde, 0.01M sodium periodate, 0.075 M L-lysine and 0.0375 M P-buffer (0.081 M Na_2HPO_4 and 0.019M NaH_2PO_4; pH 7.4)]. After washing twice with P-buffer, samples were incubated in 30% sucrose (Merck, 107687) in P-buffer for a minimum of two days. Samples were mounted in Tissue-Tek® O.C.T. Compound (Sakura, 4583) on dry ice and cut into 8 μm sections. The frozen sections were thawed for 1 h at room temperature before immunolabeling. The sections were blocked and permeabilized in 2% BSA, 0.1% Triton X-100 in PBS for 30 min at room temperature. Primary antibodies were incubated in 2% BSA in PBS overnight at +4°C. The sections were washed 3 x 10 min with PBS and incubated with the appropriate secondary antibodies (diluted in 2% BSA in PBS) for 1 h at room temperature. Sections were then washed 3 x 10 min with PBS (1:1000 DAPI in the second wash) and then 5 min with milliQ water. The sections were mounted under a glass coverslip with Mowiol® (Calbiochem) supplemented with 2.5% 1,4-diazabicyclo[2.2.2]octane (DABCO, Sigma-Aldrich), and viewed with a spinning-disk confocal microscope. The center vs. the edge of DCIS acini was determined based on the edge of the keratin-8 (KRT8) signal and the ratio between MYO10 signal intensity in these areas was quantified using Fiji.

RNA *in situ* hybridization

RNA *in situ* hybridization was performed on mouse xenograft FFPE sections and human FFPE breast tissue sections with RNAscope® 2.5 HD Detection kit (BROWN, cat no. 322300) (Advanced Cell Diagnostics) based on the manufacturer's instructions using a probe targeting the region 1262–2318 in MYO10 mRNA (RNAscope® Probe - Hs-MYO10-full, cat no. 440691). For negative and positive controls RNAscope® Negative Control Probe – DapB (cat no. 310043) and RNAscope® Positive Control Probe - Hs-PPIB (cat no. 313901) were used, respectively (Advanced Cell Diagnostics). Nuclei were labelled with hematoxylin, and samples were mounted in DPX new (Merck). Samples were imaged with a Panoramic Slide Scanner (3DHistech), and 20x (xenografts) or 40x (human tissues) images were acquired in CaseViewer software. Human images were color deconvoluted, tumor/epithelial structures were selected manually, and MYO10 mRNA (brown) and hematoxylin (blue) signals within these structures were thresholded to obtain the area of each signal using Fiji. MYO10 mRNA spot area was divided by the nuclear area to normalize cell density. The MYO10 mRNA spots at the center and the edge of the DCIS acini were quantified with automatic segmentation by training a WEKA pixel classifier (Arganda-Carreras et al., 2017). The DCIS acini outer edge was defined manually. The edge area used for quantification was automatically extracted and defined as a 20 μm band inward from the DCIS acini outer edge

Quantitative RT-PCR

Total RNA extracted using the NucleoSpin RNA Kit (Macherey-Nagel) was reverse transcribed into cDNA using the high-capacity cDNA reverse transcription kit (Applied Biosystems) according to the manufacturer's instructions. The RT-PCR reactions were performed using pre-designed single tube TaqMan gene expression assays (GAPDH: Hs03929097_g1) and were analyzed with the 7900HT fast RT-PCR System (Applied Biosystems). Data were studied using RQ Manager Software (Applied Biosystems).

Western blotting

Protein extracts were separated under denaturing conditions by SDS–PAGE and transferred to nitrocellulose membranes. Membranes were blocked for 1 h at room temperature with a blocking buffer (LI-COR Biosciences) and then incubated overnight at 4°C with the appropriate primary antibody diluted in blocking buffer. Membranes were washed with PBS and then incubated with the appropriate fluorophore-conjugated secondary antibody diluted 1:5000 in blocking buffer for 30 min. Membranes were washed in the dark and then scanned using an Odyssey infrared imaging system (LI-COR Biosciences).

Light microscopy

The spinning-disk confocal microscope used was a Marianas spinning-disk imaging system with a Yokogawa CSU-W1 scanning unit on an inverted Zeiss Axio Observer Z1 microscope controlled by SlideBook 6 (Intelligent Imaging Innovations, Inc.). Images were acquired using either an Orca Flash 4 sCMOS camera (chip size 2,048 × 2,048; Hamamatsu Photonics) or an Evolve 512 EMCCD camera (chip size 512 × 512; Photometrics). Objectives used were a 20x air objective (NA 0.8, Plan-Apochromat, Zeiss), a 40x water (NA 1.1, LD C-Apochromat, Zeiss), a 63x oil (NA 1.4, Plan-Apochromat, M27 with DIC III Prism, Zeiss) and a 100x oil (NA 1.4 oil, Plan-Apochromat, M27) objective.

The confocal microscope used was a laser scanning confocal microscope LSM880 (Zeiss) equipped with an Airyscan detector (Carl Zeiss) and a 40x oil (NA 1.4) objective. The microscope was controlled using Zen Black (2.3), and the Airyscan was used in standard super-resolution mode.

Electron microscopy

The samples were fixed with 5% glutaraldehyde in s-collidine buffer, postfixed with 1% OsO4 containing 1.5% potassium ferrocyanide, dehydrated with ethanol, and embedded using a 45359 Fluka Epoxy Embedding Medium kit. Thin sections were cut using an ultramicrotome to a thickness of 70 nm. The sections were stained using uranyl acetate and lead citrate. The sections were examined using a JEOL JEM-1400 Plus transmission electron microscope operated at 80 kV acceleration voltage.

Proliferation assay

To monitor cell proliferation *in vitro*, cells were plated at low density in a well of a six-well plate and imaged using a live-cell microscopy incubator (IncuCyte ZOOM). Growth rates were calculated using the confluency method within the IncuCyte ZOOM software.

Circular invasion assays

Cells were plated in one well of a two-well culture-insert (Ibidi, Cat Number: 80209) pre-inserted within a well of a μ-Slide 8 well (Ibidi, Cat Number: 80807). After 24 h, the culture-insert was removed, and a fibrillar collagen gel (PureCol EZ Gel) was cast. The gel was allowed to polymerize for 30 min at 37°C before normal media was added on top. Cells were left to invade for two days before fixation or live imaging.

To analyze filopodia properties, fixed samples were stained with phalloidin-488 and imaged using a spinning-disk confocal microscope (100x objective). Filopodia density and length were then automatically analyzed using the FiloQuant plug-in implemented in Fiji (Jacquemet et al., 2017; Schindelin et al., 2012).

To analyze the effect of MYO10 silencing on cell migration, shCTRL and shMYO10 cells were incubated for 2 h with 0.5 μM SiR-DNA (Lukinavičius et al., 2015) (SiR-Hoechst, Tetu-bio, Cat Number: SC007) before being imaged live for 14 h using a spinning-disk confocal microscope (20x objective, 1 picture every 10 min). Nuclei were automatically detected using the deep learning algorithm

StarDist implemented in the ZeroCostDL4Mic platform and tracked using TrackMate (von Chamier et al., 2021; Ershov et al., 2022; Fazeli et al., 2020; Schmidt et al., 2018; Tinevez et al., 2017). This custom StarDist model was trained for 100 epochs on 72 paired image patches (image dimensions: 1024x1024, patch size: 1024x1024) with a batch size of 2 and a mae loss function, using the StarDist 2D ZeroCostDL4Mic notebook (v1.12.2). The StarDist "Versatile fluorescent nuclei" model was used as a training starting point. The training was accelerated using a Tesla P100. This model generated excellent segmentation results on our test dataset (average Intersection over union > 0.96; average F1 score > 0.96) (Laine et al., 2021). The StarDist model and the training dataset used are available for download on Zenodo (Jacquemet, 2020). Cell tracks were further analyzed using the Motility Lab website (http://www.motilitylab.net/, (Wortel et al., 2019)).

To analyze the effect of MYO10 silencing on cell protrusions, shCTRL and shMYO10 cells were imaged live for a few hours using a spinning-disk confocal microscope (100x objective, 1 picture every 3 min). Images were then processed using Fiji (Schindelin et al., 2012).

To perform migration competition assays, GFP positive and negative DCIS.com cell lines were mixed in a 1:1 ratio before being plated in a circular invasion assay. Cells were imaged live for 16 h using a spinning-disk confocal microscope (20x objective, 1 picture every 10 min). For each time point, the migration edges and the GFP-positive cells were automatically segmented, and the percentage of the leading edge covered by the GFP-positive cells was then calculated.

ECM remodeling assay

To form spheroids, DCIS.com cells were seeded as single cells, in standard growth media, at a very low density (3,000 cells per well) on growth factor reduced (GFR) Matrigel-coated glass-bottom dishes (coverslip No. 0, MatTek; used for live experiments) or similarly coated glass coverslips (used for fixed samples). After 12 h, the medium was replaced by a standard growth medium supplemented with 2% (vol/vol) GFR Matrigel, and the cells were returned to the incubator. After two more days, 10 μg/ml of fluorescently labeled ECM (fibronectin or laminin-111) and 10 μM of blebbistatin, 10 μM of saracatinib, 10 μg/ml of integrin beta-1-blocking antibody AIIB2 or vehicle (DMSO) were added into the indicated cultures.

Three days after the addition of the 2% Matrigel, all the spheroids were either imaged live or fixed with 4% PFA for 20 min at room temperature, washed with PBS, and prepared for imaging. Indicated samples were permeabilized with 0.25% Triton X-100 in PBS for 10 min, blocked with immunofluorescence buffer (0.2% Triton X-100, 0.05% Tween, 0.1% BSA, and 10% horse serum in PBS) for 1.5 h, incubated with 1:100 anti-active integrin beta-1 antibody overnight at +4 °C, washed three times with the immunofluorescence buffer, incubated in the appropriate fluorophore-conjugated secondary antibody for 1 h at room temperature and washed again. Finally, all the fixed spheroids were mounted on object glasses using Mowiol-DABCO. To quantify the amount of ECM recruitment and remodeling occurring at the surface of the spheroids, 3D stacks were acquired using a spinning-disk confocal microscope (0.4 μm step size). The three middle planes from each stack were combined into SUM projections using a custom Fiji (Schindelin et al., 2012) macro. Using F-actin as a marker to indicate the spheroid outlines, the mean fluorescence intensity of exogenous ECM in an approximately 2.5 μm wide region around each spheroid was measured.

For live-cell imaging of the spheroids, a spinning-disk confocal microscope was used. Videos were denoised using the deep Learning algorithm DecoNoising (Goncharova et al., 2020) implemented within ZeroCostDL4Mic (von Chamier et al., 2021). The DecoNoising models were trained for 200 epochs directly on the images to denoise using a patch size of 80 x 80 pixels, a batch size of 4, and a virtual batch size of 20, using the DecoNoising 2D ZeroCostDL4Mic notebook (v1.12). The training was accelerated using a Tesla P100 GPU, and data augmentation was enabled.

RNA sequencing and data analyses

Tumors were dissected 25 days after inoculation and stored in an RNAlater lysis buffer (Producer). RNA was extracted from tissue (ca. < 30 mg/sample) and collected in H_2O using the Qiagen RNeasy Plus Mini kit. The quality of the total RNA samples was ensured with Agilent Bioanalyzer 2100. Sample concentration was measured with Nanodrop ND-2000, Thermo Scientific. Total RNA samples were pure and intact, and all samples had a similar quality. Bioanalyzer RIN values were > 9.4. The library preparation was started from 100 ng of total RNA.

Library preparation was done according to Illumina TruSeq® Stranded mRNA Sample Preparation Guide (part # 15031047). The high quality of the libraries was confirmed with Agilent Bioanalyzer 2100, and the concentrations were quantified with Qubit® Fluorometric Quantitation, Life Technologies. Library quality was excellent, and all samples had similar quality (fragments in the range of 200-700 bp and the average size of the fragments 250-350 bp).

The samples were normalized and pooled for the automated cluster preparation, which was carried out with the Illumina cBot station. The 8 libraries were pooled and run in one lane. The samples were sequenced with the Illumina HiSeq 3000 instrument. Paired-end sequencing with 2 x 75 bp read length was used with 8 + 8 bp dual index run. The technical quality of the HiSeq 3000 run was good, and the cluster amount was as expected. Greater than 75% of all bases above Q30 were requested. The typical yields are 260-310 x 106 paired-end or single-end reads per lane on HiSeq 3000, depending on the library type and quality. The base calling was performed using Illumina's standard bcl2fastq2 software, and automatic adapter trimming was used.

The quality of the sequencing reads was checked using the FastQC tool (v. 0.11.4) (http://www.bioinformatics.babraham.ac.uk/projects/fastqc). The reads were analyzed against both human and mouse references. First, the sequencing reads were separately aligned to human (UCSC hg38) and mouse (UCSC mm10) reference genomes, derived from the Illumina iGenomes resource (https://support.illumina.com/sequencing/sequencing_software/igenome.html), using STAR aligner (v. 2.5.2b) (Dobin et al., 2013). For

mouse reference, the reads that also aligned to human reference were removed using XenofilteR (v. 0.99.0) (Kluin et al., 2018). Next, the uniquely aligned reads were associated with RefSeq gene models using Subread (v. 1.5.1) (Liao et al., 2014) for each organism.

QUANTIFICATION AND STATISTICAL ANALYSIS

For RNAseq data, normalization and statistical testing were carried out with R (v. 3.4.1) and Bioconductor (v. 3.6) (Gentleman et al., 2004), using edgeR (McCarthy et al., 2012) and Limma packages (Ritchie et al., 2015). In each comparison, genes with a mean RPKM expression value below 0.125 in both sample groups were filtered out, and the normalized expression values were voom transformed before statistical testing. An absolute fold-change above two and a false discovery rate (FDR) smaller than 0.01 or 0.05 were required to select the differentially expressed genes.

For other data, randomization tests were performed using PlotsOfDifferences (Goedhart, 2019). Dot plots were generated using PlotsOfData (Postma and Goedhart, 2019), Volcano Plots were generated using VolcaNoseR (Goedhart and Luijsterburg, 2020), and SuperPlots were generated using SuperPlotsOfData (Goedhart, 2021; Lord et al., 2020). Other statistical tests were performed using GraphPad Prism software. The Student's t-test (unpaired, two-tailed) was used for normally distributed data. The non-parametric Mann–Whitney U-test was used when two non-normally distributed groups were compared. Fisher's exact test was used for the analysis of contingency tables. Data representation and n-numbers for each graph are indicated in figure legends.